Characterization of droplet sizes in large scale oil–water flow downstream from a globe valve

L.D. Paolinelli*, A. Rashedi, J. Yao

Institute for Corrosion and Multiphase Technology, Department of Chemical & Biomolecular Engineering, Ohio University, 342 W. State Street, Athens, OH 45701, USA

ABSTRACT

Oil–water dispersed flows produced at valves or restrictions are very common in industry. For example, crude oil desalting processes normally use dispersion valves to mix the dilution water. In this case, the knowledge of dispersed droplet sizes is crucial for the design and optimum control of the process. However, little work has been devoted to characterize and model droplet sizes produced in industrial-type valves. The present work studies water droplet sizes produced by the passage of oil–water flow through a globe valve mounted in a large scale flow loop of 0.1 m internal diameter. Experiments were performed under different pressure drops across the globe valve, and different oil and water flow rates. Produced water droplet sizes were measured *in situ* downstream from the globe valve location using particle video microscopy. Droplet sizes were compared with theoretical scales for turbulent and viscous break-up. The effect of the volume fraction of dispersed phase on droplet size was also examined. In addition, droplet size distributions were analyzed and fitted using known statistical functions.

© 2017 Elsevier Ltd. All rights reserved.

1. Introduction

Multiphase flow involving two immiscible liquids is commonly found in industrial processes. For example, oil–water dispersed flow can exist in upstream as well as downstream operations of the oil industry. These dispersions can be caused by the disruption of the water or the oil phase into droplets due to the intrinsic turbulence of the mixture flow in pipes, or due to the shear/turbulence produced at valves. Valves are commonly used to reduce the pressure of flow lines (e.g., choke valves) or specifically to disperse one fluid into the other. Extensive work has been devoted to study droplet sizes in liquid–liquid flow with the aim of characterizing the dispersion and/or emulsion behavior in pipes (Angeli and Hewitt, 2000; Collins and Knudsen, 1970; Hanzevack and Demetriou, 1989; Hesketh et al., 1991; Hesketh et al., 1987; Karabelas, 1978; Kubie and Gardner, 1977; Simmons and Azzopardi, 2001; Sleicher, 1962; Vielma et al., 2008; van der Zande and van der Broek, 1998). On the contrary, less information about droplet sizes produced at restrictions or valves can be found in the literature (Fossen and Schümann, 2017; Galinat et al., 2007; Galinat et al., 2005; Jansen et al., 2001; Percy and Sleicher, 1983; van der Zande and van der Broek, 1998; van der Zande et al., 1999). This is of particular interest in the oil production and processing in-

dustry. For example, crude oil delivered to refineries usually contains residual entrained salt water; this must be removed to avoid operational and integrity problems in refinery facilities (Al-Otaibi et al., 2003; Stewart and Arnold, 2011). In general, the crude oil stream is washed with fresh water to dilute the residual salt water. Subsequently, this water is separated and removed from the crude oil, in the final step of what is called the desalting process. A basic desalting process consists of the following steps: dilution water injection into the oil stream; mixing of the injected water by some device, which in general is achieved with a valve (e.g., a globe valve); and residence of the water-in-oil mixture in a desalter, which separates the water from the crude oil. The process is optimized to dissolve as much residual salt as possible from the crude oil, as well as remove most of the remaining water content whilst maintaining high crude oil flow rates (Al-Otaibi et al., 2003; Vafajoo et al., 2012). A key parameter to achieve these goals is the water droplet sizes produced during the mixing process. Small droplet sizes promote higher efficiency on the salt dissolution process due to their larger surface/volume ratio and number. However, small droplet sizes can also pose a problem when separating the water at the desalter due to their diminished settling velocity and higher chance of stabilizing emulsions (Eow et al., 2001). Despite the importance of characterization and modeling of droplet sizes produced by valves, minimal experimental work has been reported in the literature.

Percy and Sleicher (1983) studied droplet break-up in liquid–liquid flow in a pipe of 38.1 mm inner diameter with con-

Notations

A	cross sectional area of the pipe, m^2
A_o	area of the opening of the globe valve, m^2
c_o	orifice or constriction coefficient, dimensionless
C_H	constant used in Brauner's model, dimensionless
$Ca_{s,\,crit}$	critical capillary number for droplet break-up in simple shear flow, dimensionless
$Ca_{e,\,crit}$	critical capillary number for droplet break-up in elongational shear flow, dimensionless
d	droplet size, m – μm
d_{max}	maximum droplet size, m – μm
d_{32}	Sauter mean diameter, m – μm
d_{50}	mean droplet size corresponding to $V = 0.5$, m – μm
d_{98}	droplet size corresponding to $V = 0.98$, m – μm
$\bar{d}$	mean droplet size of the log-normal distribution, m – μm
d^*	characteristic droplet size of the Rosin–Rammler distribution (corresponding to $V = 0.63$), m – μm
D	pipe diameter, m
D_o	orifice diameter of a pipe constriction, m
$D_{o,\,eq}$	equivalent orifice diameter for the valve opening constriction, m
D_s	globe valve seat diameter, m
f	friction factor, dimensionless
f_d	lowest natural frequency of a droplet, s^{-1}
f_e	specific frequency of the turbulent velocity fluctuations, s^{-1}
$f(\lambda)$	Taylor's function, dimensionless
h	displacement of the globe valve actuator measured from the fully closed position, m
h_{max}	maximum displacement of the globe valve actuator measured from the fully closed position, m
l	length of the chamfer at the valve seat, m
l_e	length scale of eddies with frequency f_e, m – μm
l_K	Kolmogorov length scale, m – μm
l_{max}	length scale of the largest eddies that follow Eq. (2), m – μm
n	exponent of the Rosin–Rammler distribution, dimensionless
Re_o	Reynolds number at the valve opening
S_o	perimeter of the annular opening of the globe valve, m
t	width of the annular opening of the globe valve, m
t_b	droplet break-up time, s
$t_{b,\,e}$	droplet break-up time for elongational flow, s
$t_{b,\,s}$	droplet break-up time for simple shear flow, s
t_e	eddy turnover time, s
$t_{r,\,e}$	time that droplets reside under maximum elongation stress at the globe valve opening, s
$t_{r,\,s}$	time that droplets reside under maximum shear stress at the globe valve opening, s
t_b'	dimensionless break-up time
$\overline{u'^2}$	mean value of the product of velocity fluctuations with length scale similar to d_{max}, m^2/s^2
U_m	mixture flow velocity based on the unrestricted pipe, m/s
U_o	flow velocity at the valve opening, m/s
U_c	velocity of the continuous phase based on the unrestricted pipe, m/s
U_{sc}	superficial velocity of the continuous phase based on the unrestricted pipe, m/s
V	cumulative volume fraction of droplets, dimensionless
V_{ct}	fixed control volume where the pressure of fluid mixture flow drops abruptly due to the valve restriction and then recovers to a permanent value, m^3
V_{valve}	total internal volume of the valve from flange to flange, m^3
We_{crit}	critical Weber number for turbulent droplet break-up, dimensionless
We'_{crit}	Levich's modified critical Weber number for turbulent droplet break-up, dimensionless

Greek letters

α	angle between the symmetry axis of the actuator and the conical surface of the globe valve piston, rad
β	ratio between the orifice or restriction diameter and the pipe diameter, dimensionless
β_{eq}	equivalent diameter ratio for the globe valve opening restriction, dimensionless
$\dot{\gamma}$	shear rate of the continuous phase flow, s^{-1}
$\dot{\gamma}_{max}$	maximum shear rate of the flow at the globe valve opening, s^{-1}
ΔP	pressure drop across a restriction or a valve, Pa
ΔP_{max}	maximum pressure drop across a restriction or a valve, Pa
ΔP_{perm}	permanent pressure drop across a restriction or a valve, Pa
ϵ	energy dissipation rate per unit of mass of the continuous phase, W/kg
ϵ_{valve}	mean energy dissipation rate produced by the globe valve, W/kg
ε_d	volumetric fraction of dispersed phase, dimensionless
$\dot{\varepsilon}$	extensional velocity gradient of the continuous phase flow, s^{-1}
λ	ratio between the dynamic viscosity of the dispersed and continuous phases, dimensionless
μ_c	dynamic viscosity of the continuous phase, Pa s
μ_d	dynamic viscosity of the dispersed phase, Pa s
ρ_c	density of the continuous phase, kg/m^3
ρ_d	density of the dispersed phase, kg/m^3
ρ_m	density of fluid mixture, kg/m^3
σ	interfacial liquid–liquid tension, N/m
σ_{LN}	standard deviation of the log-normal distribution, dimensionless

centric orifice plate constrictions of different diameters. Break-up probability of single droplets passing through the orifice was well correlated with a Weber number based on the maximum pressure drop across the restriction. However, maximum droplet sizes were not compared with classic turbulent break-up models (e.g., Hinze, 1955), or neither with viscous shear break-up criteria (Grace, 1982). Van der Zande et al. (1999) mimic oil–water flow through a choke valve using calibrated orifices as constrictions in 4.5 mm and 15.25 mm inner-diameter pipes to produce oil-in-water dispersions. The size scale of the droplets measured downstream the orifice was found to be proportional to the $-2/5$ power of the mean energy dissipation rate of the flow at the constriction and increased significantly with the dispersed phase viscosity. Jansen et al. (2001) also empirically modeled the flow of several crude oil–brine mixtures through a choke valve using calibrated orifices as constrictions in a pipe of 4.8 mm inner diameter. They found that homogeneous and stable water-in-oil emulsions

were formed if a certain threshold value of power per unit of mass was dissipated in the flow, depending on the type of crude oil and the oil/water ratio. Besides, it was stated that the diameter of the produced water droplets could be explained in the framework of classic turbulent and viscous break-up theories. Galinat et al. studied droplet break-up probability of single droplets passing through an orifice restriction in liquid–liquid 30 mm inner-diameter pipe flow in diluted dispersions (Galinat et al., 2005) and also in dispersions with up to 20% of dispersed phase holdup (Galinat et al., 2007). They found that the break-up probability could be modeled as a function of a global Weber number based on the maximum pressure drop across the orifice, similarly to the findings of Percy and Sleicher. However, for the largest tested drop concentration (20%), break-up probability could not be fully determined by the global Weber number, which was related to the modification of the volume of the regions of high turbulence in the flow. Mitre et al. (2014) reported an experimental and theoretical study on the evolution of droplet size distributions in water-in-crude oil emulsions through a small scale valve-like element of 25 mm² of unrestricted cross section. They performed population balance calculations to model the droplet size distribution produced after the valve element using an inertial droplet break-up model, modified to account for droplet sizes similar to the Kolmogorov length scale, since most of the generated droplets were smaller than this magnitude. Recently, Fossen and Schümann (2017) studied droplet sizes produced downstream of a butterfly valve in large scale oil–water flow (0.1 m pipe diameter) with different pressure drops across the valve and different oil and water flow rates. They found that pressure drop determined the droplet size downstream from the valve restriction and that the flow rate had a much lower effect on the droplet size. The obtained droplets sizes were compared with the turbulent break-up models of Percy and Sleicher as well as Hinze, obtaining better fit with the latter. There is little data in the literature of droplet sizes in water-in-oil dispersions produced in industrial valves under operating conditions (e.g., pressure drop, oil and water flow rates) similar to the ones used in desalting processes.

The aim of this work is to study the water droplet sizes produced by the passage of oil–water flow through a globe valve mounted in a large scale flow loop of 0.1 m internal diameter. Experiments were performed for different pressure drops across the globe valve, and different oil and water flow rates. Homogeneous water-in-oil dispersions were produced downstream from the globe valve in all the experimental conditions, and water droplet sizes were measured from images of the multiphase flow taken *in situ* using the particle video microscopy technique. Droplet sizes were compared with theoretical scales for turbulent and viscous break-up. The effect of the volume fraction of dispersed phase on droplet size was also examined. Besides, droplet size distributions were analyzed and fitted using known statistical functions.

2. Theory

A brief theoretical description of maximum size scales for the different droplet break-up phenomena that are relevant to the present case study is given as follows.

2.1. Turbulent droplet break-up

One of the most known and used models to predict maximum droplet size in turbulent liquid–liquid flow was introduced by Hinze (1955). The model assumes that the equilibrium maximum droplet size of the dispersed phase is controlled by its mechanical stability against the dynamic pressure forces exerted by the turbulent motion of the surrounding continuous phase around it. Therefore, droplet break-up is likely to occur when droplets are larger than a critical size. When the internal viscous forces in the

droplet are low enough to be neglected, the Hinze concept can be written using the Young-Laplace equation as:

$$\frac{1}{2}\rho_c\overline{u'^2} \propto \frac{4\sigma}{d_{max}} \tag{1}$$

where ρ_c is the density of the continuous phase, σ is the interfacial liquid–liquid tension, d_{max} is the maximum stable dispersed phase droplet size, and $\overline{u'^2}$ is the mean value of the product of velocity fluctuations with length scale similar to d_{max}. This average quantity can be estimated considering isotropic turbulence as (Batchelor, 1951):

$$\overline{u'^2} \cong 2(\epsilon d_{max})^{2/3} \tag{2}$$

where ϵ is the energy dissipation rate per unit of mass of the continuous phase. Finally, Hinze introduced the following expression to estimate d_{max} in liquid–liquid turbulent flow:

$$d_{max} = 0.725\left(\frac{\sigma}{\rho_c}\right)^{3/5}\epsilon^{-2/5} \tag{3}$$

where the constant 0.725 was determined by fitting Clay's experimental data (Clay, 1940) with a standard deviation of 0.315. The amount of dispersed phase used in Clay's experiments ranged from 0.9% to 4.8% in volume. Therefore, Hinze's analysis is considered to be suitable for diluted dispersions. Eq. (3) is valid provided that $l_K \ll d_{max} < l_{max}$, where l_K is the Kolmogorov length scale that approximately represents the smallest size of turbulent structures (eddies) in the continuous phase flow:

$$l_K = \left(\frac{\mu_c^3}{\rho_c^3\epsilon}\right)^{1/4} \tag{4}$$

where μ_c is the dynamic viscosity of the continuous phase; and l_{max} is the length scale of the largest eddies that follow Eq. (2). For example, in the case of pipe flow, this value has been reported to be approximately one tenth of the pipe diameter ($l_{max} \sim 0.1D$) (Kubie and Gardner, 1977).

Hesketh et al. (1987) included the effect of the dispersed phase density to predict the maximum stable droplet size by using a modified critical Weber number proposed by Levich (1962):

$$We'_{crit} = We_{crit}\left(\frac{\rho_d}{\rho_c}\right)^{1/3} = \frac{2\rho_c\epsilon^{2/3}d_{max}^{5/3}}{\sigma}\left(\frac{\rho_d}{\rho_c}\right)^{1/3} \tag{5}$$

where We_{crit} is the critical Weber number, and ρ_d is the density of the dispersed phase. The modified critical Weber number (We'_{crit}) was found to be around 1 for droplets as well as bubbles in pipe flow.

An analogous model for mechanical instability of dispersed phase droplets in turbulent flow was proposed by Sevik and Park (1973). Here, the mechanical instability of the droplet is given when the frequency of the perturbing turbulent fluctuation coincides with the natural frequency of the droplet at its lowest normal oscillation mode. The specific frequency of the turbulent velocity fluctuations is estimated as the inverse of the eddy turnover time:

$$f_e = t_e^{-1} \cong \frac{\epsilon^{1/3}}{l_e^{2/3}} \tag{6}$$

where l_e is the length scale of eddies with frequency f_e.

The lowest natural frequency of a droplet can be approximated using the formula offered by Lamb (1932) for an inviscid, negligibly viscous, fluid sphere inside another immiscible inviscid fluid (using $n = 2$):

$$f_d = \frac{1}{2\pi}\left(\frac{8(n-1)n(n+1)(n+2)\sigma}{[(n+1)\rho_d + n\rho_c]d^3}\right)^{1/2} \tag{7}$$

where d is the droplet diameter.

Combining Eqs. (6) and (7) then setting the length scale of the perturbing eddy (in Eq. (6)) and the droplet size (in Eq. (7)) as the maximum stable droplet size (d_{max}) leads to:

$$d_{max} = \left(\frac{48}{\pi^2\left(3\frac{\rho_d}{\rho_c} + 2\right)}\right)^{3/5}\left(\frac{\sigma}{\rho_c}\right)^{3/5}\epsilon^{-2/5} \tag{8}$$

It is worth noting that Eq. (8) presents the same form as the Hinze expression (Eq. (3)) but instead of a constant it contains a function of the continuous and dispersed phase densities. In the case of liquid–liquid flow where the densities of the continuous and the dispersed phase are similar ($\rho_c \sim \rho_d$), the value of the mentioned function is ~0.98, which is close to the average constant value found by Hinze.

There are other semi-empirical models particularly developed to determine the maximum length scale of dispersed droplets produced downstream of an orifice in turbulent liquid–liquid pipe flow. Percy and Sleicher (1983) assumed that droplet break-up only occurs if a critical value of Weber number, which is based on the stress from the acceleration of the fluid though the orifice, is exceeded:

$$We_{crit} = \frac{\Delta P\,d_{max}^2}{D_o\sigma} \tag{9}$$

where d_{max} is the maximum droplet diameter that can survive the applied stress without breaking up, D_o is the orifice diameter, and ΔP is the pressure drop across the orifice. From the fitting of experimental data, Percy and Sleicher came up with the following expression:

$$d_{max} = 3.1\left(\frac{D_o\sigma}{\Delta P_{max}}\right)^{1/2} \tag{10}$$

Galinat et al. (2005) used the same approach and found a similar constant value of 2.8 from their experimental data. van der Zande and van der Broek (1998) better fit their experimental data with a constant value of 5.4. This larger constant value was associated with the high viscosities of the oils used as the dispersed phase. In this case, high Ohnesorge or viscosity numbers are computed for the droplets, their internal viscous forces are not negligible and larger external stresses are demanded for their effective break-up (Galinat et al., 2005; van der Zande and van der Broek, 1998).

The pressure drop (ΔP) in expressions (9) and (10) can be conveniently expressed as a function of the mixture velocity of the fluids in the unrestricted pipe (U_m) using the *vena contracta* formulation (Galinat et al., 2005; Jansen et al., 2001):

$$\Delta P_{max} = \frac{1}{c_o^2}\frac{1}{2}\rho_m U_m^2\left(\frac{1}{\beta^4} - 1\right) \tag{11}$$

$$\Delta P_{perm} = \Delta P_{max}\left(1 - \beta^2\right) \tag{12}$$

where ΔP_{max} is the maximum pressure drop given just downstream from the restriction, ΔP_{perm} is the permanent pressure drop across the restriction, c_o is the orifice coefficient, β is the ratio between the orifice diameter and the pipe diameter (D_o/D), ρ_m is the mixture density:

$$\rho_m = \rho_d\varepsilon_d + \rho_c(1 - \varepsilon_d) \tag{13}$$

and U_m is the mixture velocity that can be calculated from the superficial velocity of the continuous phase (U_{sc}) as:

$$U_m = \frac{U_{sc}}{(1 - \varepsilon_d)} \tag{14}$$

where ε_d is the volumetric fraction of dispersed phase.

2.2. Droplet break-up in simple shear and elongational flow

Despite of the fact that the present work relates to turbulent flow through a globe valve, droplet break-up mechanisms other than those aforementioned can also be present, affecting the scale of the produced droplet sizes. For example, the high shear and acceleration of the flow generated at the valve constriction may in some cases dominate the maximum droplet size, and need to be considered. In some cases, to evaluate what is the controlling break-up mechanism is not trivial since turbulent, shear and elongation effects can act simultaneously and may lead to similar maximum droplet sizes depending on the local flow characteristics.

Droplet break-up in simple shear flow is characterized by means of the critical capillary number defined by Grace (1982) as:

$$Ca_{s,crit} = \frac{\mu_c|\dot{\gamma}|\,d_{max}\,f(\lambda)}{2\sigma} \tag{15}$$

where d_{max} is the maximum droplet diameter that can endure the applied stress without breaking up, $\dot{\gamma}$ is the shear rate of the continuous phase flow, and $f(\lambda)$ is a function introduced by Taylor of the ratio between the dynamic viscosity of the dispersed and continuous phases ($\lambda = \mu_d/\mu_c$) (Taylor, 1932). For water-in-oil dispersions the function $f(\lambda)$ can be dismissed since its value ranges from 1 to 1.1 for $\lambda \sim 0$ to $\lambda = 1$, respectively. Critical capillary number values for droplet break-up in simple shear flow have been obtained empirically as a function of the viscosity ratio λ, and can be found elsewhere (Grace, 1982).

Droplet break-up in elongational flow can also be assessed by means of a critical capillary number (Grace, 1982):

$$Ca_{e,crit} = \frac{\mu_c\dot{\varepsilon}\,d_{max}}{2\sigma} \tag{16}$$

where $\dot{\varepsilon}$ is the extensional rate or extensional velocity gradient of the continuous phase flow. It was found that the critical capillary number for droplet breakup in elongational hyperbolic flow can be several times lower than for simple shear flow depending on the viscosity ratio λ (Bentley and Leal, 1986; Grace, 1982).

3. Experimental

3.1. Flow apparatus and experimental conditions

The two-phase flow experiments were conducted in a large-scale multiphase flow loop. A schematic layout of the flow loop is shown in Fig. 1. The main part of the loop consists of a 30 m long, 0.1 m internal diameter (ID) flow line mounted on a steel rig structure. The loop consists of two parallel legs of PVC and stainless steel pipes connected by a 180° bend. Oil and water liquids are pumped separately from the individual storage tanks into the 0.1 m ID main line by progressive cavity pumps. Flow rates of oil and water are monitored independently by flow meters with a maximum uncertainty of 10%. Water is injected into the main line at a T-junction through a perpendicular 0.05 m ID secondary line. The oil–water mixture flows for approximately 50 pipe diameters in the upstream leg before reaching the test section, used for final mixing and *in-situ* visualization of generated water droplet sizes. This distance from the water injection section to the test section is due to the location of the first flange available downstream.

Upon exiting the downstream leg of the flow loop, the mixture is directed to a calming section of 0.3 m ID and 7.5 m long for pre-separation of the oil and water and subsequently to a separator of 2 m³ capacity with mesh and plate droplet coalescers; this equipment is described in detail elsewhere (Cai et al., 2012). The residence time of the fluids at the separator is about 3 and 5 min for the maximum and minimum mixture flow rates employed of 0.013 and 0.009 m³/s; respectively. The separated oil and water streams
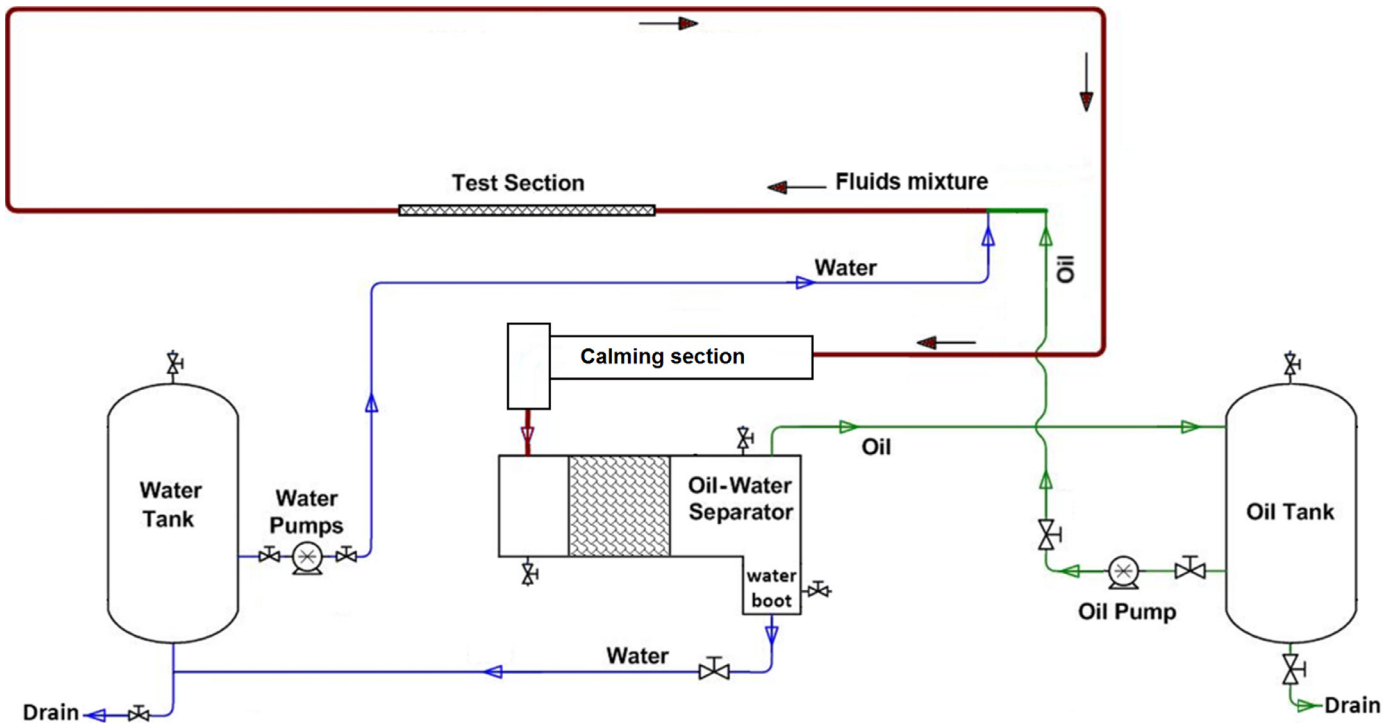
Fig. 1. Schematic layout of the 0.1 m ID flow loop used for oil–water flow.

Table 1
Experimental conditions.

Water volume fractions	From 0.5 to 16%
Oil–water mixture velocities	1.1, 1.4 and 1.6 m/s
Reynolds numbers	9900–14,400
Pressure drop across the globe valve	62, 83, 103, 124 and 165 kPa
Temperature	From 20 to 25 °C

Fig. 2. Schematic of the 0.1 m ID globe valve.

are then returned to their respective storage tanks (1.2 m³ capacity each) for further recirculation.

The fluids used in the experiments were Isopar V® as the oil phase (density: 810 kg/m³ and viscosity: 0.009 Pa s at 25 °C) and 0.1 wt% NaCl (prepared using deionized water). The oil–water interfacial tension was 0.049 N/m at 25 °C. Isopar V® is a clear saturated paraffinic oil, which facilitates the visualization of entrained water droplets at moderate illumination settings. Water dispersions in Isopar V® oil are unstable and undergo rapid separation.

Table 1 lists the water volume fractions range used, average oil–water mixture velocities, pressure drops across the mixing valve of the test section and temperatures of the performed flow experiments. The pressure drop across the valve was incrementally adjusted by gradually closing the opening of the globe valve.

3.2. Test section design and instrumentation

The main test section consisted of a mixing valve and upstream and downstream stainless steel test spools with ports for instrumentation. The mixing valve was a standard flanged stainless steel 0.1 m ID globe valve class 150 with a geometrical configuration as shown in Fig. 2. Fig. 3 shows the detailed geometry of the valve seat and the actuator piston. For any actuator displacement (h, measured from the fully closed position), an annular opening of width t allows the passage of the fluid mixture:

$$t = h\sin\alpha \tag{17}$$

where α is the angle between the central symmetry axis of the actuator and the generatrix of the piston conical surface that faces
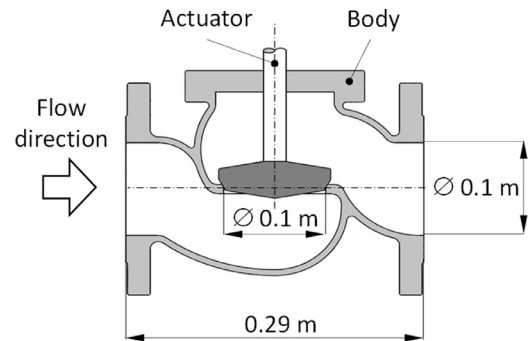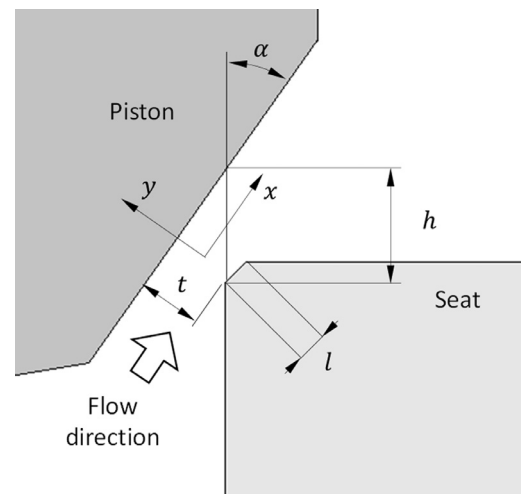

Fig. 3. Schematic of the seat and the actuator piston of the 0.1 m ID globe valve.

Main test section

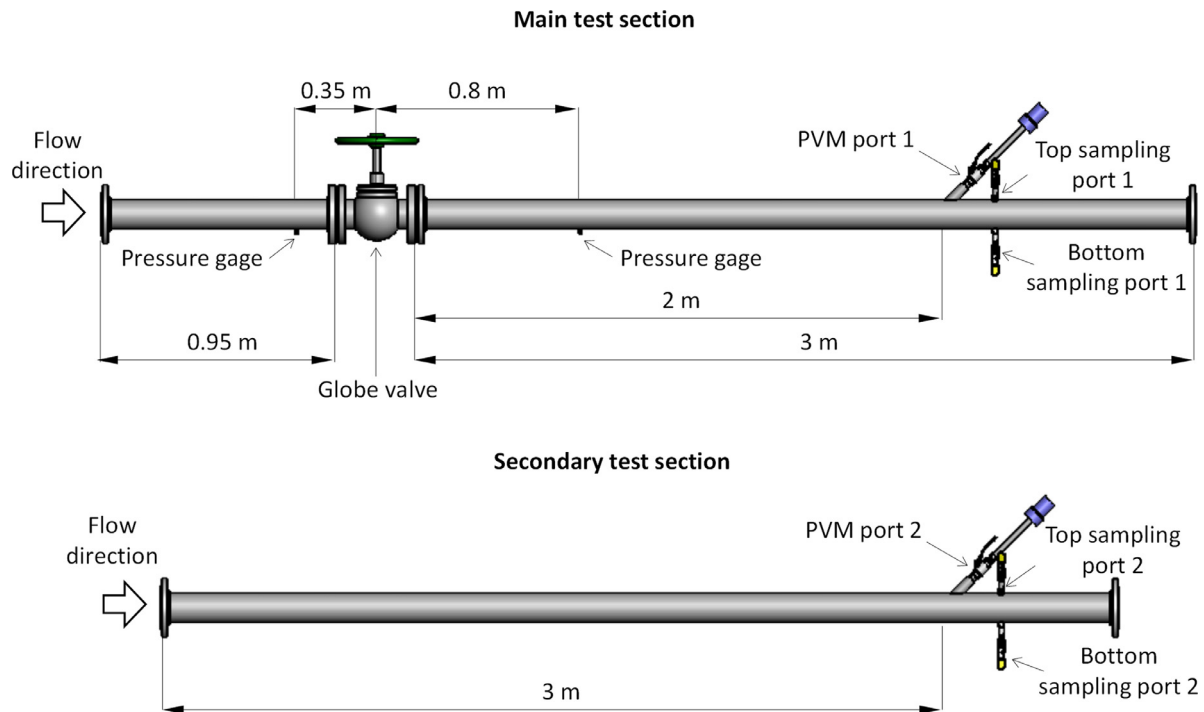

Secondary test section

Fig. 4. Schematic of the test section.

the valve seat, which was measured as 29°. The perimeter of the annular opening is proportional to the seat diameter (D_s):

$$S_o = \pi D_s \tag{18}$$

D_s is similar to the pipe internal diameter ($D = 0.1$ m) as is usually found in most of the globe valves of the used class. Then, the opening area is approximated as:

$$A_o = S_o t \tag{19}$$

The valve seat has a 45° chamfer of length (l), 1 mm.

Fig. 4 shows a schematic of the whole test section that consisted of two parts. The main section was specially designed to generate a uniform water-in-oil mixture by controlling the pressure drop across the globe valve. Both upstream and downstream pipe spools (before and after the globe valve, respectively) contained pressure taps equipped with a differential pressure transducer (accuracy 0.8 kPa) connected to a computer interface. Pressure drop was monitored with a sampling rate of 1 s and averaged in time. Measured pressure drop fluctuations were not larger than 5% of the measured average pressure drop value. The location of the downstream pressure tap was selected to be 8 pipe diameters from the valve actuator. This distance was long enough to avoid the well-known maximum pressure drop peak produced just downstream of the valve constriction (Hwang and Pal, 1998; Pal and Hwang, 1999).

The downstream pipe spool was equipped with a port for the particle video microscopy (PVM) instrument used for *in situ* droplet visualization. This port allowed instrument insertion at 45° of incidence to achieve good visualization of the droplets in the oncoming flow and to produce a continuous flushing of the transparent optical window to avoid droplet sticking. The PVM equipment used was a V819 Mettler Toledo®, which is able to visualize droplets or particles from around 10 to 1000 μm. More detailed information about the PVM working principle can be found elsewhere (Boxall et al., 2010). The secondary test section only consisted of a straight pipe with PVM equipment insertion port and sampling ports, and was placed just downstream from the main test section (Fig. 4).

The main droplet visualization port (shown as PVM port 1 in Fig. 4) was located at a distance of about 22 pipe diameters downstream from the valve actuator. This length assured full mixing and uniformity of the dispersed oil–water flow before monitoring dispersed water droplets. Another similar visualization port (shown as PVM port 2 in Fig. 4) was located 4 m downstream from the main visualization port in order to characterize the evolution of produced droplet sizes along the straight pipe section.

In order to characterize the oil–water flow pattern without the effect of the globe valve, the main test section was replaced by a straight 0.1 m ID pipe spool. Pictures of the oil–water flow were taken at a clear section located just at the end of the secondary test section, about 140 pipe diameters downstream from the water injection section. Fig. 5 shows pictures of the flow patterns observed from the side of the clear section for mixture velocities of 1.1 m/s, 1.4 m/s and 1.6 m/s, and water volume content of 0.8%. Flow is stratified with some water globules formed at the oil–water interface at 1.1 m/s mixture velocity. Semi-dispersed flow is observed for the larger mixture velocities. It can also be noticed that, for all the tested mixture velocities, larger water droplets reach sizes above 3 mm. These large droplets are about one order of magnitude larger than the maximum droplet sizes produced by the globe valve, as will be discussed further in the results section. The large scale difference between droplet sizes produced by the straight pipe flow and the globe valve flow is not surprising since the mean power dissipated in the fluid in the latter is about 500 times larger for the present conditions.

The test section was also equipped with top and bottom fluid sampling ports of 0.01 m ID at a distance of 24 pipe diameters and 64 pipe diameters downstream from the globe valve (sampling ports 1 and 2 in Fig. 4, respectively, just beside the locations for droplet visualization) to check volumetric water concentration in the produced mixture; and thus, the degree of uniformity of the generated water-in-oil mixture. The Karl-Fischer volumetric titration method was used on the fluid samples. At least 2 fluid samples were taken from each top and bottom ports at both locations of the test section for characterization.
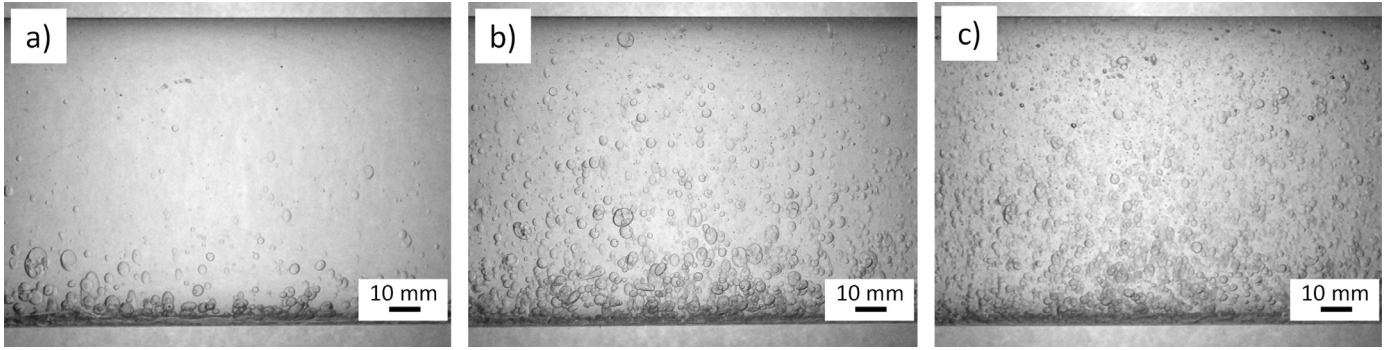
Fig. 5. Flow patterns observed from the side of a clear section in straight pipe flow (without valve) for mixture velocities of 1.1 m/s (a), 1.4 m/s (b) and 1.6 m/s (c), and water volume content of 0.8%.

Table 2
Examples of measured water volume content at different sampling locations for globe valve and straight pipe flow.

U_m (m/s)	Injected water vol. cont. (%)	Globe valve					Straight pipe	
		ΔP (kPa)	Sampling location #1		Sampling location #2		Sampling location #2	
			Bottom (%)	Top (%)	Bottom (%)	Top (%)	Bottom (%)	Top (%) x10^{-2}
1.1	5	83	5.5 ± 0.4	5 ± 0.4	5.75 ± 0.5	5 ± 0.4	100	0
1.1	11	83	11.5 ± 0.9	10.5 ± 0.8	16 ± 3	10.5 ± 0.8	100	0
1.4	5	165	5.1 ± 0.4	5 ± 0.4	5 ± 0.4	5 ± 0.4	94 ± 3	0.6 ± 0.5
1.6	5	124	5.5 ± 0.5	5.25 ± 0.4	5.7 ± 0.5	5.5 ± 0.4	89 ± 7	5 ± 0.8

Table 2 lists examples of measured water concentrations for globe valve flow and straight pipe flow for single experimental runs with injected water volume contents of 5% and 11% and different mixture velocities. Water distribution at the pipe cross-section is always inhomogeneous in straight pipe flow, showing water contents larger than 80% at the pipe bottom and very low or zero concentration at the pipe top. In the case of the globe valve flow, the measured water concentration at the sampling location 1, which is closest to the mixing valve, is similar at both the bottom and top of the pipe. The same behavior is seen for all the experimental conditions run with the globe valve, where the differences between measured bottom and top water concentrations never exceeded 15%. Therefore, it is assumed that the produced mixtures were mostly homogeneous across the pipe section at the monitoring location 1. On the other hand, water concentrations measured at the sampling location 2 (about 6 m downstream from the mixing valve) can show significant differences between the bottom and top of the pipe. In particular, this occurs at conditions where the pressure drop across the valve is below 124 kPa and the water volume content is larger than 6%. In these cases, produced water droplets tend to be larger and their settling at the pipe bottom due to gravity occurs faster; particularly for the lowest mixture velocity used (1.1 m/s). The analysis of water droplet sizes monitored at location 2 of the test section can be definitely biased by the fact that a significant percentage of larger droplets could have settled at the pipe bottom. Moreover, droplet coalescence can also be a factor to consider, as will be discussed later.

Fluid samples were also taken from the bottom of the water-free oil stream upon exiting the oil–water separator. The measured residual water contents were always below 13% of the total injected water volume fraction for each run. This contamination, due to the incomplete separation of very small droplets (in general, estimated below 30 μm diameter), could have somewhat biased the measured droplet size distributions. However, this error does not significantly affect mean droplet size and other parameters as regards statistical functions used to characterize droplet size distributions, discussed further below.

3.3. Globe valve flow characterization

Table 3 lists geometric and flow parameters of interest for the different tested conditions. The pressure drop across the globe valve (ΔP) and the mixture (oil and water) velocity (U_m) were kept constant for each experimental run. The opening height (h) was estimated as the difference between the distances from a reference point at the valve actuator shaft to a horizontal reference plane at the top of the valve body, measured when operating and when the valve is fully closed. The uncertainty on these measurements is estimated as 0.5 mm. Valve opening is expressed as the ratio between h and the maximum opening height possible (h_{max}). No adjustment of the opening height was necessary to keep the pressure drop constant when the water volume content was increased from about 0.5% up to 16%. The opening gap width (t) is calculated using Eq. (17). The flow velocity at the valve opening (U_o) is estimated as:

$$U_o = U_m \frac{A}{A_o} \tag{20}$$

where A_o is the valve opening area as in Eq. (19), and A is the cross sectional area of the pipe.

The globe valve flow can be characterized as a flow through an orifice where the equivalent diameter of the orifice is estimated as:

$$D_{o,eq} = D\beta_{eq} \tag{21}$$

where β_{eq} is the equivalent diameter ratio calculated as:

$$\beta_{eq} = \left(\frac{A_o}{A} \right)^{1/2} \tag{22}$$

The mean energy dissipation rate per unit of mass of the continuous phase passing through the globe valve can be expressed as:

$$\epsilon_{valve} = \frac{A \, \Delta P \, U_c}{V_{ct} \, \rho_c \, (1 - \varepsilon_d)} \tag{23}$$

Table 3
Flow and geometric parameters for the different experimental conditions.

ΔP (kPa)	U_m (m/s)	ϵ (W/kg)	h (mm)	h/h_{max} (%)	t (mm)	U_o (m/s)	$D_{o,\,eq}$ (m)	β_{eq}
62	1.1	125	5.1	9.5	2.4	11.3	0.031	0.31
83	1.1	165	4.4	8.4	2.1	12.9	0.029	0.29
103	1.1	205	3.8	7.2	1.8	15.0	0.027	0.27
124	1.6	375	5.3	9.9	2.5	15.8	0.032	0.32
165	1.4	430	4.2	7.9	2.0	17.3	0.028	0.28

where U_c is the velocity of the continuous phase in the unrestricted pipe that can be considered equal to the mixture velocity (U_m) for dispersed flow, V_{ct} is the fixed control volume where the pressure of fluid mixture flow drops abruptly due to the valve restriction and then recovers to a permanent value. Computational fluid dynamics (CFD) results on flow patterns in similar globe valve geometries (Chern et al., 2013; Palau-Salvador et al., 2004; Rammohan et al., 2009; Yang et al., 2011) indicate that pressure starts dropping suddenly near the seat of the valve piston. Taking this into account, half of the internal globe valve volume ($V_{valve}/2$, measured as 2×10^{-3} m^3) is included into V_{ct}. According to the experimental work of Pal and Hwang (Hwang and Pal, 1998; Pal and Hwang, 1999) on oil–water emulsion flows through globe valves, full pressure recovery occurs at about 6 pipe diameters downstream from the valve actuator axis. Therefore, V_{ct} is estimated as $V_{valve}/2$ plus the portion of pipe volume left to achieve a distance of 6 pipe diameters from the valve actuator axis.

The maximum shear rate is given at the valve opening where the mixture flow passes between the seat and piston surfaces, and is approximated as in a turbulent flow between parallel plates:

$$\dot{\gamma}_{max} \cong \mu_c^{-1} \left(\frac{1}{2} \rho_c f U_o^2 \right) \tag{24}$$

where f is the Fanning friction factor (Patel and Head, 1969):

$$f = 0.0376 Re_o^{-1/6} \tag{25}$$

and:

$$Re_o = \frac{\rho_c U_o t}{\mu_c} \tag{26}$$

The mean mixture flow velocity close to the entrance of the valve opening can be approximated as a function of the coordinate x with origin at the valve opening position (Fig. 3):

$$U_o(x) \cong \frac{U_m\, A}{S_o(t - x \tan \alpha)} = \frac{U_o\, t}{(t - x \tan \alpha)} \tag{27}$$

Note that this equation is only valid for small negative increments of the coordinate x. Then, the maximum mean extensional rate can be obtained from differentiating Eq. (27) in x and specifying at the valve opening:

$$\dot{\varepsilon} = \frac{\partial U_o}{\partial x}\bigg|_{x \sim 0} \cong \frac{U_m\, A \tan \alpha}{S_o t^2} = \frac{U_o \tan \alpha}{t} \tag{28}$$

3.4. Droplet image capture and digital processing

At least 3 runs were performed for each experimental condition. For each experimental run, the oil–water flow was stabilized at the desired condition (pressure drop, and oil and water flow velocities) for about 10 min before imaging the dispersed water droplets. The image capture was performed at the center of the pipe section. About 500 high-quality pictures were captured per run with an elapsed time of 1 s between pictures.

Pictures of water droplets were digitally processed using ImageJ® software. Fig. 6 shows an example of an unprocessed picture
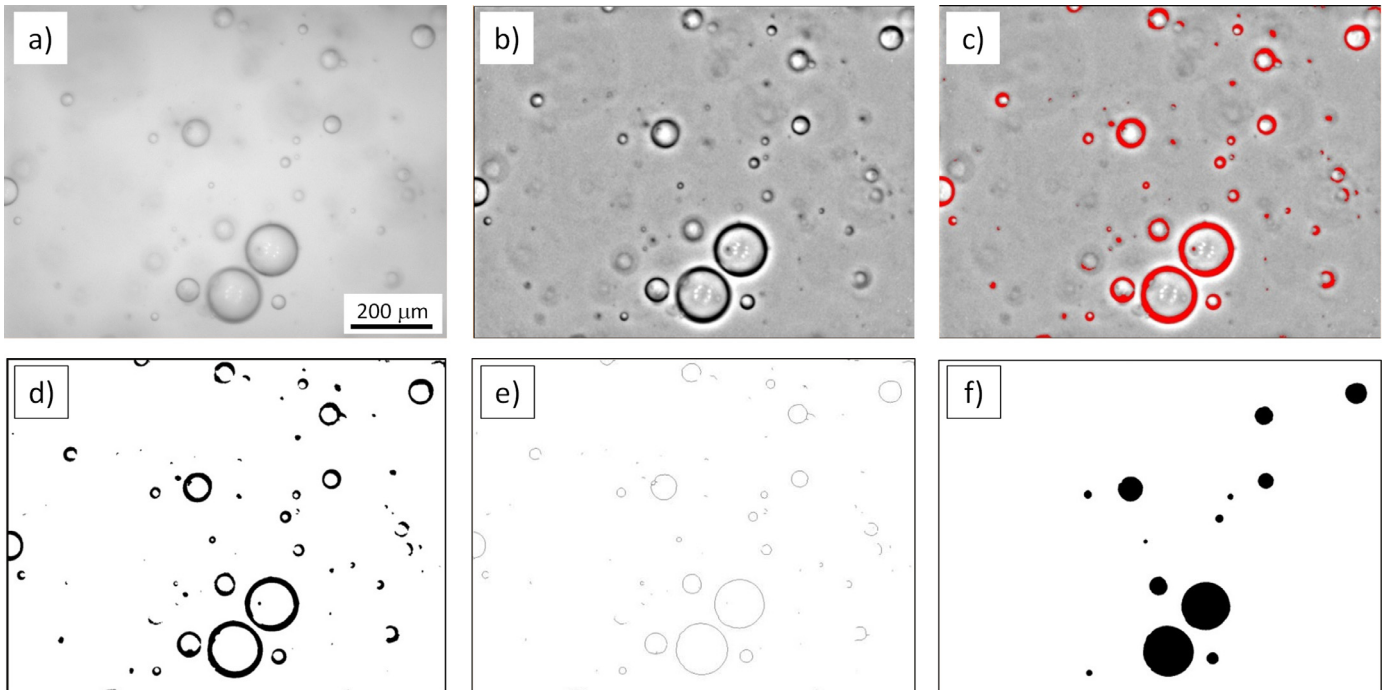

Fig. 6. Example of an unprocessed PVM picture (a) and its processing procedure consisting of: band-pass filtering (b), contrast enhancement (c, d), droplet contour identification (e), count of droplets with closed contours (f) and size measuring.
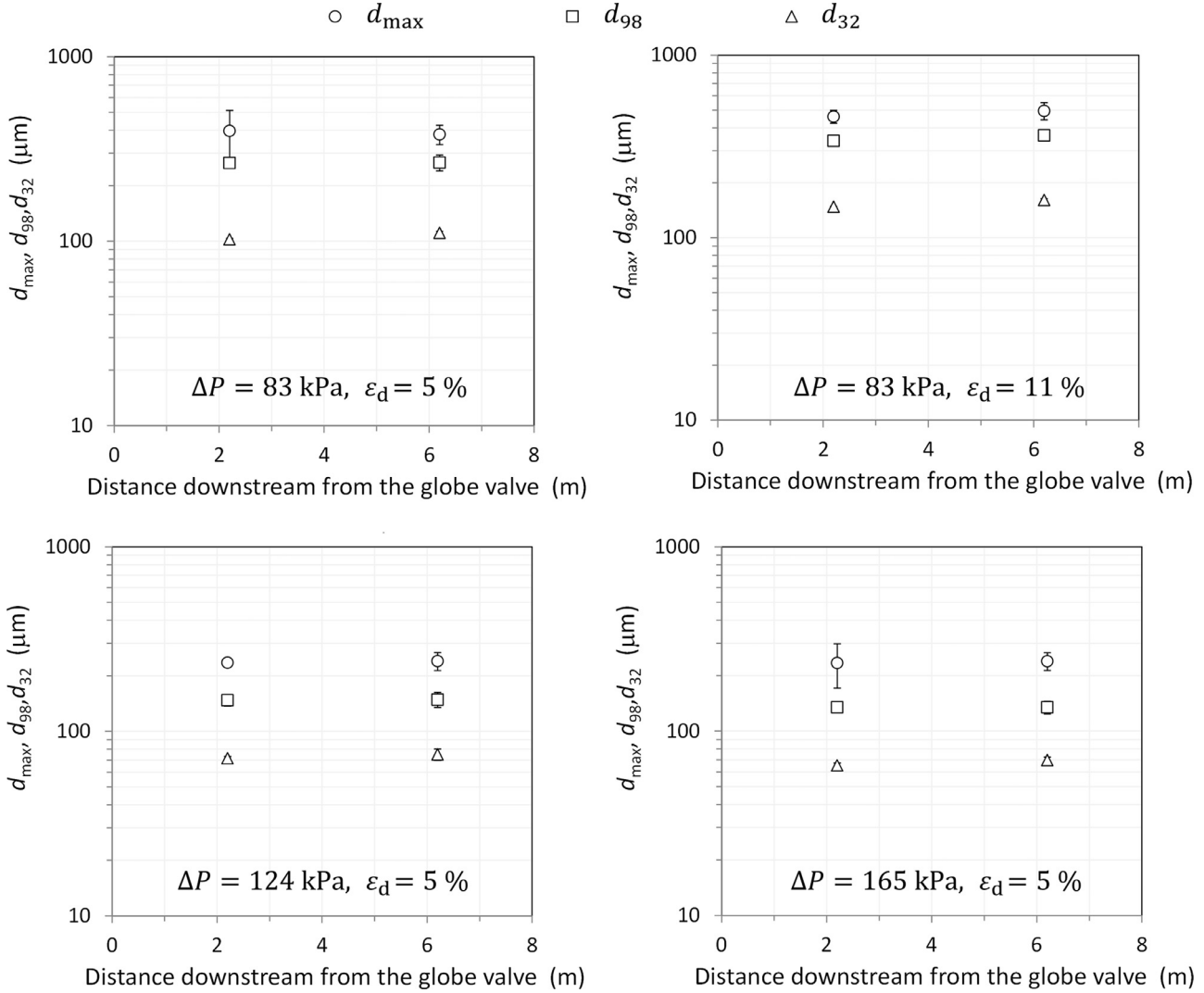
Fig. 7. Measured d_{max}, d_{98} and d_{32} values in function of the distance downstream from the globe valve for different flow conditions.

(Fig. 6a) and its processing procedure consisting of band-pass filtering (Fig. 6b), contrast enhancement (Fig. 6c and d), droplet contour identification (Fig. 6e), count of droplets with closed contours (Fig. 6f), and size measurement. In general, no fewer than 10,000 droplets were processed per experimental run. The estimated uncertainty of the droplet diameter measurement was smaller than 10% for droplet sizes larger than about 30 μm, and smaller than 20% for lower droplet sizes. When determining maximum water droplet sizes, the results from the digital image processing were crosschecked by manual inspection of each individual picture to minimize the error.

4. Results and discussion

4.1. Effect of the distance downstream from the globe valve on droplet sizes

Water droplet sizes were measured at both monitoring locations 1 and 2 of the test section for a reduced set of conditions in order to observe the evolution of droplets produced by the globe valve flow downstream in a straight pipe. Fig. 7 shows maximum droplet size (d_{max}), the droplet size corresponding to 98% of the cumulative volume of droplets of smaller sizes (d_{98}), and the mean

droplet size in terms of Sauter mean diameter:

$$d_{32} = \frac{\sum d_i^3 \, n_i}{\sum d_i^2 \, n_i} \tag{29}$$

where n_i is the number of droplets of size d_i. The data in Fig. 7 and upcoming graphs in this work are shown as average values from independent experimental runs, and error bars represent the standard deviation.

For an injected water volume fraction of 5%, d_{max} and d_{98} do not vary between the monitoring locations 1 and 2. However, mean droplet size (d_{32}) increases on average about 8%, 5% and 7% for pressure drops across the mixing valve of 83 kPa, 124 kPa and 165 kPa, respectively. This effect is related to the coalescence between droplets of medium sizes that are measured with more frequency and, in consequence, are more susceptible to collision and agglomeration. Droplet break-up is not considered to occur since the intensity of turbulent flow in the straight pipe is not enough to disrupt the droplets produced by the globe valve, as can be inferred from the flow patterns found in straight pipe flow (Fig. 5). For the larger injected water volume content of 11%, d_{max}, d_{98} and d_{32} increase between locations 1 and 2 by about 7.5%, 9% and 7% on average, respectively. In this case, maximum droplet size and mean droplet size are similarly affected by coalescence, probably
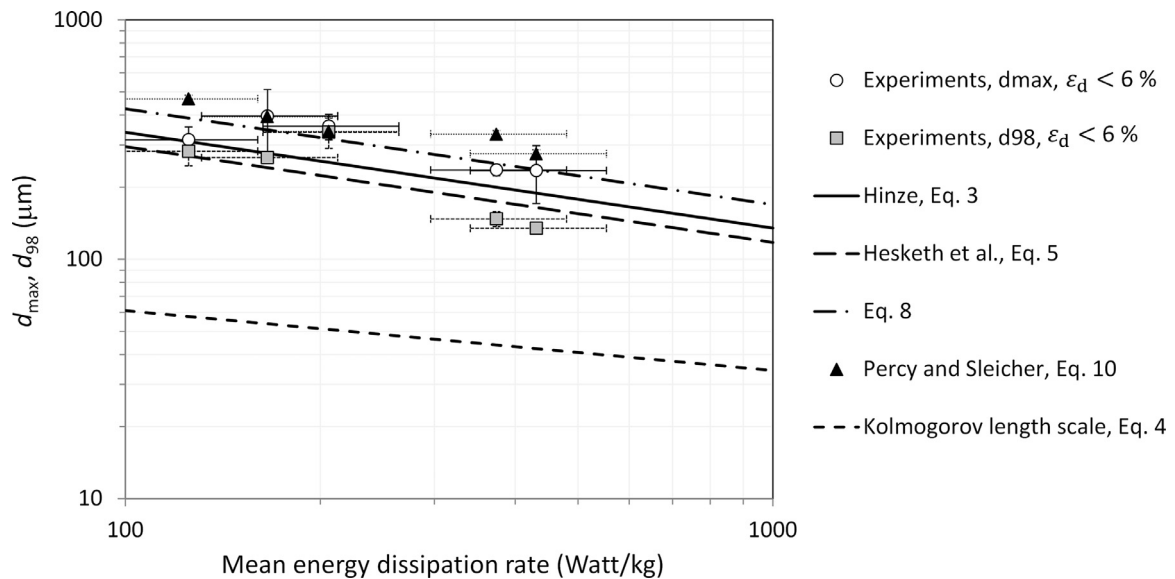
Fig. 8. Measured d_{max} and d_{98} values as a function of the mean energy dissipation rate. Comparison with theoretical maximum droplet sizes for turbulent break-up and Kolmogorov's scale. Water volume fractions are lower than 6%.

due to the fact that the dispersion is more crowded and collisions between droplets are more frequent for all the available droplet population. It is worth reminding that water distribution at the pipe cross-section at location 2 showed significant differences between the top and the bottom of the pipe for 11% of injected water volume content. Therefore, water droplets measured at the center of the pipe at location 2 might not be representative of the whole pipe cross-section.

In general, the relative growth of mean droplet sizes between locations 1 and 2 does not surpass 9% for the conditions shown in Fig. 7. This corresponds to a growth rate of around 2.2% per meter of pipe. In the remainder of this work, analyzed water droplets were only monitored at location 1, which is situated at about 2.1 m downstream from the valve actuator.

Droplet break-up and coalescence (if significant) intrinsic to the valve effect dominate at the pipe region downstream from the valve where pressure is still lower than its recovering value (estimated about 6 pipe diameters long), but then generated water droplets could be affected by similar coalescence rates as seen above when flowing along the 1.55 m straight pipe distance left before reaching location 1. However, this effect is considered insignificant since the expected relative size growth would not be larger than 3.5%.

It is worth mentioning that the model oil and water used in this work generate dispersions that separate quickly. This behavior is rarely found in industrial processes with crude oil, where coalescence of water droplets is difficult.

4.2. Measured maximum and mean droplet sizes, comparison with theoretical length and time scales

Fig. 8 shows experimental maximum droplet size (d_{max}) and d_{98} values as a function of the mean energy dissipation rate for small water volume fractions (lower than 6%), as well as different lines and scattered points (black triangles) representing theoretical length scales for turbulent break-up. Each d_{max} value (hollow circles) and d_{98} value (grey squares) shown corresponds to the average of values obtained from independent experimental runs, the error bars represent the standard deviation. The error bars shown on the mean energy dissipation rate values consider the er-

ror propagation due to uncertainty as regards the estimation of the pressure recovery distance downstream from the valve (± 0.1 m), which is the major error factor, and measurement of the pressure drop across the valve ($\pm 5\%$) and the velocity of the continuous phase ($\pm 5\%$).

The found maximum droplet sizes are about 10 times larger than the Kolmogorov length scale (Eq. (4), short-dashed line). This allows the assessment of inertial models for turbulent break-up. In this context, the Hinze model (Eq. (3), solid line), the Hesketh et al. model (Eq. (5), long-dashed line) and the model described in Eq. (8) (dash-dot line) represent well the decreasing trend of the maximum droplet size with the mean energy dissipation rate of the continuous phase flow (ϵ). The Hinze expression underpredicts d_{max} by 12% on average with a standard deviation of 18%. The equation offered by Hesketh underpredicts d_{max} by 24% on average with a standard deviation of 15%. While Eq. (8), developed from matching the resonance frequency of the droplets with the frequency of the perturbing eddies, overpredicts the maximum droplet size by 10% on average with a standard deviation of 22%.

On the other hand, the model of Percy and Sleicher (Eq. (10)) was also evaluated using the equivalent orifice diameter ($D_{o, eq}$) and the equivalent diameter ratio (β_{eq}) calculated from the measured valve opening gap using Eqs. (21) and (22), respectively. The maximum pressure drop across the globe valve (ΔP_{max}) was estimated from the measured permanent pressure drop (ΔP_{perm}) by using Eq. (12). The estimated maximum droplet size values are somewhat in agreement with the experimental data (black triangles, Fig. 8), over predicting by 30% on average with a standard deviation of 30%. If the constant value of 2.8 found by (Galinat et al. (2005) is used in Eq. (10), the estimation of d_{max} improves, over predicting only by 17% with a standard deviation of 26%.

The time scale for droplet break-up in turbulent flow can be associated with the first mode natural oscillation frequency of the droplet (Eq. (7)) as suggested by Hesketh et al. (1991). On the other hand, Coulaloglou and Tavlarides (1977) estimated the break-up time to be of the order of the turnover time of perturbing eddies with length scale similar to the droplet size. The model described by Eq. (8) (dash-dot line in Fig. 8) complies with both perspectives, although it was formulated with a different reasoning.
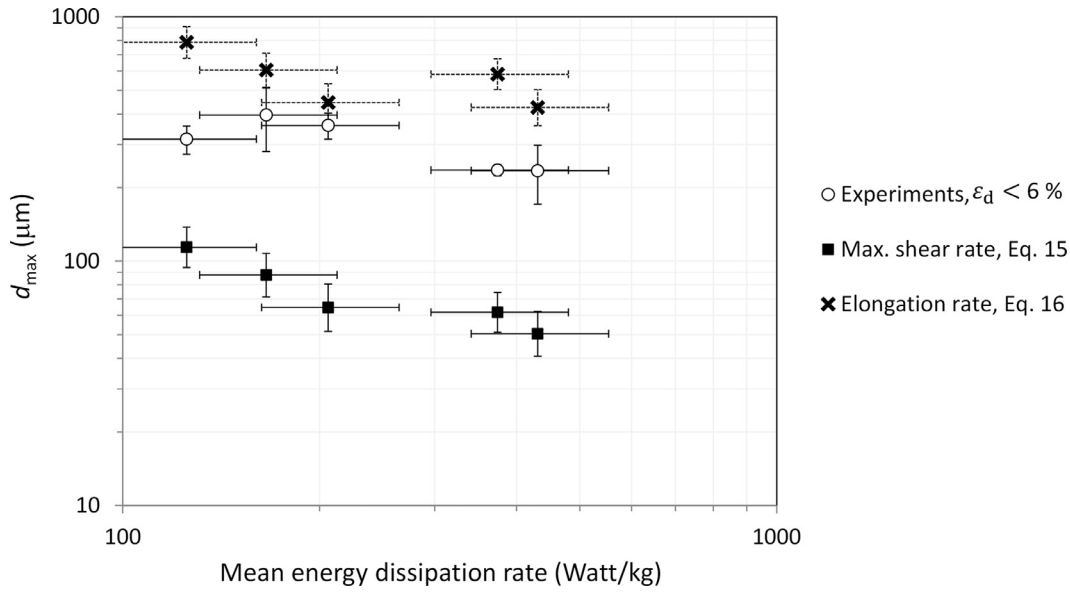
Fig. 9. Measured maximum water droplet size as a function of the mean energy dissipation rate. Comparison with theoretical critical droplet sizes for simple shear and elongation break-up. Water volume fractions are lower than 6%.

Measured d_{98} values are from about 10% to 40% lower than found maximum droplet size values, showing larger differences at the conditions where mean energy dissipation rate is larger.

In order to evaluate if shear and elongational break-up mechanisms also contributed to control the maximum droplet sizes produced by the globe valve, estimations of typical critical droplet sizes were performed. In the case of droplet break-up by simple shear, the critical droplet size was calculated using Eq. (15) based on a critical capillary number $Ca_{s,\,crit} = 0.6$ (obtained from Grace, 1982 for the actual viscosity ratio $\lambda = 0.11$), and the maximum shear rate given at the valve opening ($\dot{\gamma}_{max}$, Eq. (24)). Fig. 9 shows the estimated maximum droplet size for simple shear as black squares, error bars consider the error propagation from the calculation of the shear rate. The estimated maximum droplet sizes are about 4 times smaller than the experimental values in some of the tested conditions. For droplet break-up in elongational flow, the critical droplet size was calculated using Eq. (16) based on a critical capillary number $Ca_{e,\,crit} = 0.18$ (obtained from Grace, 1982 or Bentley and Leal, 1986 at $\lambda = 0.11$), and the elongation rate estimated at the valve opening ($\dot{\varepsilon}$, Eq. (28)). The predicted maximum droplet sizes for elongational flow (black crosses in Fig. 9) are in general larger than the experimental values with differences up to a factor of 3.

The time scales of the droplet break-up in both simple shear and elongational flow must additionally be estimated to evaluate if these processes were feasible in the actual case study. The droplet break-up time (t_b) for shear and elongation splitting mechanisms can be predicted from the correlations provided by Grace (1982). Here, the dimensionless critical burst time, defined as:

$$t_b' = \frac{t_b\, \sigma}{d_{max}\, \mu_c} \tag{30}$$

is correlated with the viscosity ratio λ. For the present ratio $\lambda = 0.11$, the values of t_b' are 10 and 3 for simple shear and elongational flow, respectively. The time that droplets are subjected to maximum shear stress in the flow at the valve opening (residence time) is approximated as:

$$t_{r,s} \cong \frac{l}{U_o} \tag{31}$$

where droplets are assumed to travel at a velocity similar to U_o, and l is the length of the chamfer at the valve seat (Fig. 3), which

is equal to 1 mm. On the other hand, the time that droplets are exposed to the critical extensional stress in the flow is estimated as the time that it takes for droplets to move from an upstream position close to the valve opening (defined by the coordinate x in Fig. 3) where the extensional rate ($\dot{\varepsilon}$) is about 80% of its maximum value (x_{80}), to the position where $\dot{\varepsilon}$ is maximum (valve opening, $x\sim0$). This distance is obtained differentiating Eq. (27) in x; then, the residence time can be approximated as the quotient between its value and the mean flow velocity close to the valve opening ($x_{80}^{-1} \int_0^{x_{80}} U_o(x)dx$):

$$t_{r,e} \cong \frac{t\left(1 - \frac{1}{\sqrt{0.80}}\right)^2}{U_o \tan\alpha\, \ln\left(\frac{1}{\sqrt{0.80}}\right)} \tag{32}$$

Table 4 lists the calculated droplet break-up and residence times as well as the shear and extensional rates for the different tested conditions, the reported error values are estimated from the uncertainty on the measured continuous phase velocity (±5%) and the displacement of the globe valve actuator (±0.25 mm). The estimated break-up times are about 2 times and one order of magnitude larger than the time that droplets reside in the flow at critical conditions for simple shear and elongation configurations, respectively. This would indicate that these break-up mechanisms are unlikely to dominate maximum droplet size in the tested conditions, and would explain why the typical maximum droplet scales calculated from Eqs. (15) and (16) (Fig. 9) do not agree well with all the experimental data.

From the analysis above, water droplet sizes produced by the globe valve in the tested conditions seem to be mostly controlled by turbulent break-up. Moreover, all the introduced models to predict maximum droplet size in turbulent flow agree well with the available experimental data. It is worth pointing out that the Percy and Sleicher model (Eq. (10)) developed for an orifice constriction can be successfully used provided the geometry of the valve opening is known, calculating the equivalent orifice diameter ($D_{o,\,eq}$, Eq. (21)) and the equivalent diameter ratio (β_{eq}, Eq. (22)).

Fig. 10 shows the Sauter mean diameter (d_{32}). The mean droplet diameter (hollow circles) tends to decrease with the mean energy dissipation rate similarly to d_{max}. The average d_{max}/d_{32} ratio is about 3.7. This number is higher than the d_{max}/d_{32} ratio of 2.2 and

Table 4

Droplet break-up and residence and times calculated for simple shear and elongation mechanisms at different tested conditions.

ΔP (kPa)	ϵ (W/kg)	Shear flow			Elongational flow		
		$\dot{\gamma}_{max}$ (1/s) $\times 10^3$	$t_{r,\,s}$ (s) $\times 10^{-6}$	$t_{b,\,s}$ (s) $\times 10^{-6}$	$\dot{\varepsilon}$ (1/s) $\times 10^3$	$t_{r,\,e}$ (s) $\times 10^{-6}$	$t_{b,\,e}$ (s) $\times 10^{-6}$
62	125	58.5 ± 11	88.6 ± 8.8	205 ± 39	2.5 ± 0.38	49.1 ± 7.3	424 ± 63
83	165	76 ± 16	77.8 ± 8.2	158 ± 32	3.3 ± 0.54	37.8 ± 6.2	327 ± 53
103	205	103 ± 23	66.7 ± 7.7	116 ± 26	4.4 ± 0.82	27.8 ± 5.1	241 ± 44
124	375	108 ± 20	63.2 ± 6.2	111 ± 21	3.4 ± 0.5	36.3 ± 5.3	314 ± 46
165	430	132 ± 28	57.8 ± 6.3	90.8 ± 19	4.7 ± 0.8	26.6 ± 4.5	230 ± 39
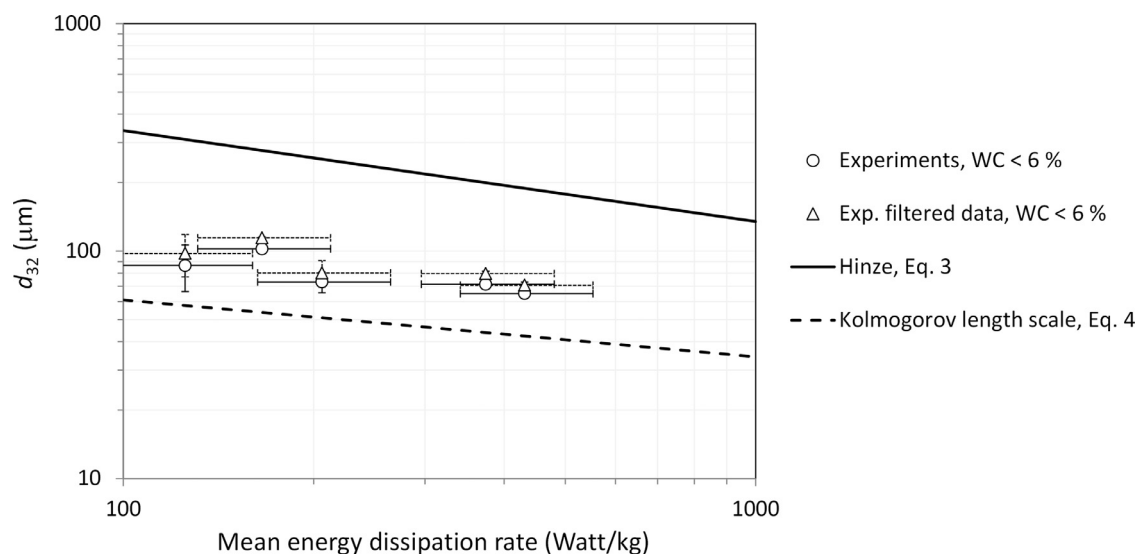
Fig. 10. Measured Sauter mean diameter as a function of the mean energy dissipation rate. Comparison with Kolmogorov's and Hinze's scales. Water volume fractions are lower than 6%.

2.6 found by Angeli and Hewitt (2000) and Karabelas (1978) in oil–water pipe flow, respectively. However, it is close to the ratio of 3.6 reported by Simmons and Azzopardi (2001) also obtained in oil–water pipe flow. Other works performed in liquid–liquid dispersions in stirred tanks show d_{max}/d_{32} ratios from 1.8 to 4 (Calabrese et al., 1986; Lovick et al., 2005; Sprow, 1967), which are in the range of the present findings.

As aforementioned, residual water contents always below 13% of the total injected water volume fraction were measured upon exiting the oil–water separator for each experimental run. In order to quantify the impact of this contamination, characteristic of very small droplets, on droplet size distribution the mean droplet sizes were recalculated removing the volume fraction measured as contamination from the smaller droplet size population relating to each run. The mean droplet sizes recalculated using the "filtered" data are shown in Fig. 10 as hollow triangles. The recalculated d_{32} values show a small increase of about 10% in all the experimental conditions compared to the d_{32} values calculated using the entire droplet population. Another characteristic droplet size such as d_{98} was also analyzed in the same way showing an even smaller increase of about 2% in all the experimental conditions.

The actual contamination of the clean oil stream with unseparated water may have been smaller than the volumetric content measured at the exit of the oil–water separator, since some of the residual water could have settled at the oil tank bottom before recirculation. Unfortunately, this cannot be confirmed since no sampling port was available for fluid sampling at the oil injection line. Given the small differences found between mean droplet sizes analyzed with and without considering residual water contamination as well as the uncertainty on the actual value of contaminating

water concentrations, characteristic water droplet sizes and droplet distributions shown in the remainder of this work will be only based on the entire measured droplet population.

4.3. Effect of dispersed phase volume fraction on droplet size

Figs. 11 and 12 show the measured maximum droplet sizes and d_{98} values, respectively, as a function of the water volume fraction for all the tested conditions. These values are normalized by the magnitude $(\sigma/\rho_c)^{3/5}\epsilon^{-2/5}$, which accounts for the influence of turbulent flow as well as the fluid properties; see Eqs. (3) and (8) above. The error bars on the water volume fraction correspond to the maximum and minimum average values measured at location 1.

Despite the scattered nature of the experimental data, it is observed that maximum droplet size tends to grow with the water volume fraction (ε_d). For example, the maximum droplet sizes produced at water volume fractions of around 15% are about 2 times larger than those generated at water volume fractions of about 1% or less. The Hinze model (dashed line in Figs. 11 and 12) fails to describe the maximum droplet size behavior for water volume fractions larger than about 6%. This is as expected; since the model was developed using data attained with low dispersed phase fractions, as stated above. The drop size growth with the content of the dispersed phase has been associated with either a gradual decrease in the effective turbulent stress in the flow, commonly called turbulence damping, or droplet coalescence (Brauner, 2001; Mlynek and Resnick, 1972; Pacek et al., 1998). Regarding the modeling of this phenomenon, Brauner (2001) proposed an extension of the Hinze model to estimate the maximum stable droplet
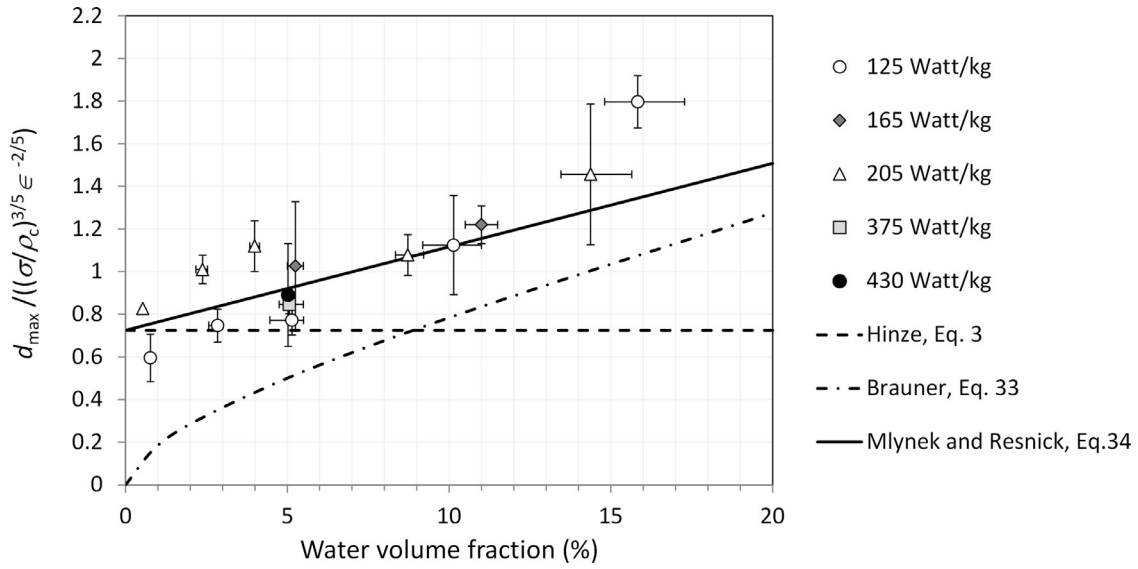
Fig. 11. Measured normalized d_{max} as a function of the water volume fraction. Comparison with models.
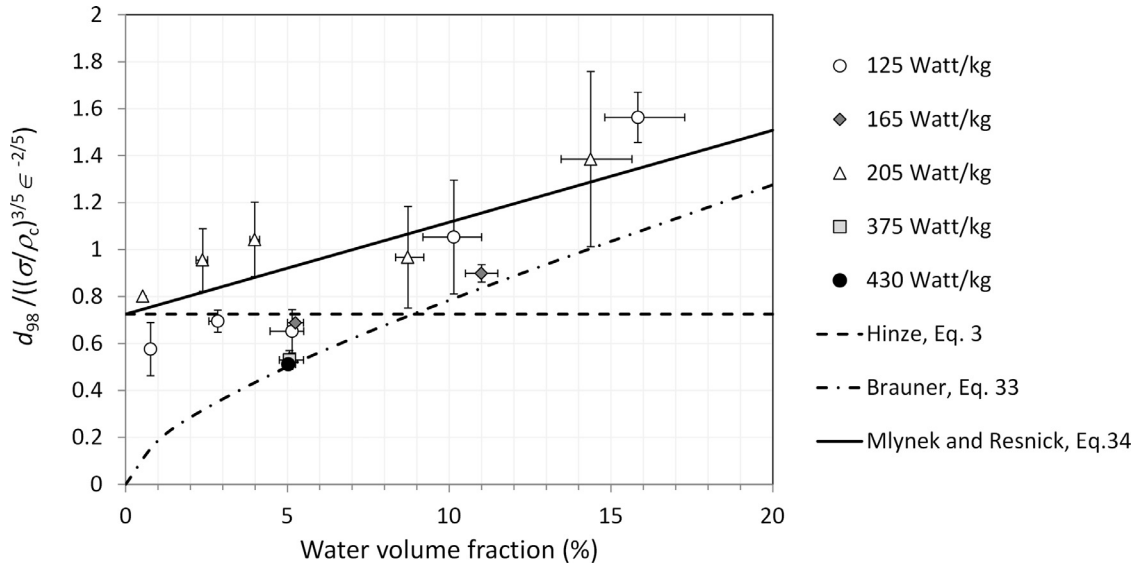

Fig. 12. Measured normalized d_{98} as a function of the water volume fraction. Comparison with models.

size in dense dispersions based on an energy balance affected by the flow rates of the continuous and dispersed phases. The author postulated that as coalescence takes place in dense dispersions, the incoming flow of the continuous phase should carry sufficient turbulent energy to disrupt the tendency to coalesce and disperse the other phase. Therefore, the maximum droplet size of the dispersed phase is calculated as:

$$d_{max} = \left(6C_H \frac{\varepsilon_d}{(1-\varepsilon_d)}\right)^{3/5} \left(\frac{\sigma}{\rho_c}\right)^{3/5} \epsilon^{-2/5} \qquad (33)$$

where C_H is a constant of the order of 1. Eq. (33) describes somewhat well the slope of d_{max} growth for water volume fractions larger than 5% (dash-dot line in Figs. 11 and 12). However, it under predicts d_{max} values by an average of about 30%. A drawback of Eq. (33) is that it is unsuitable for diluted dispersions (maximum droplet size tends to zero).

Mlynek and Resnick (1972) presented the following empirical multiplication factor to describe the effect of the dispersed phase

volume fraction (ε_d) on droplet sizes in turbulent flow:

$$f(\varepsilon_d) = (1 + 5.4\,\varepsilon_d) \qquad (34)$$

This expression is very convenient since it can be used for any value of ε_d. In Figs. 11 and 12, Eq. (34) is plotted using Hinze's droplet size as reference value for low or negligible water content (solid line), showing fair agreement with the trend of the experimental data.

Fig. 13 shows the normalized values of measured Sauter mean diameter as a function of the water volume fraction for all the tested conditions. The mean droplet size values also tend to increase with the water volume fraction. Eq. (34) multiplied by a constant of value 0.187 is found to best fit the experimental data (solid line).

4.4. Droplet size distributions

Figs. 14 and 15 show examples of droplet size distribution in terms of cumulative volume (V) and volume density ($\frac{dV}{dd}$), respectively, for different mean energy dissipation rates in the continuous
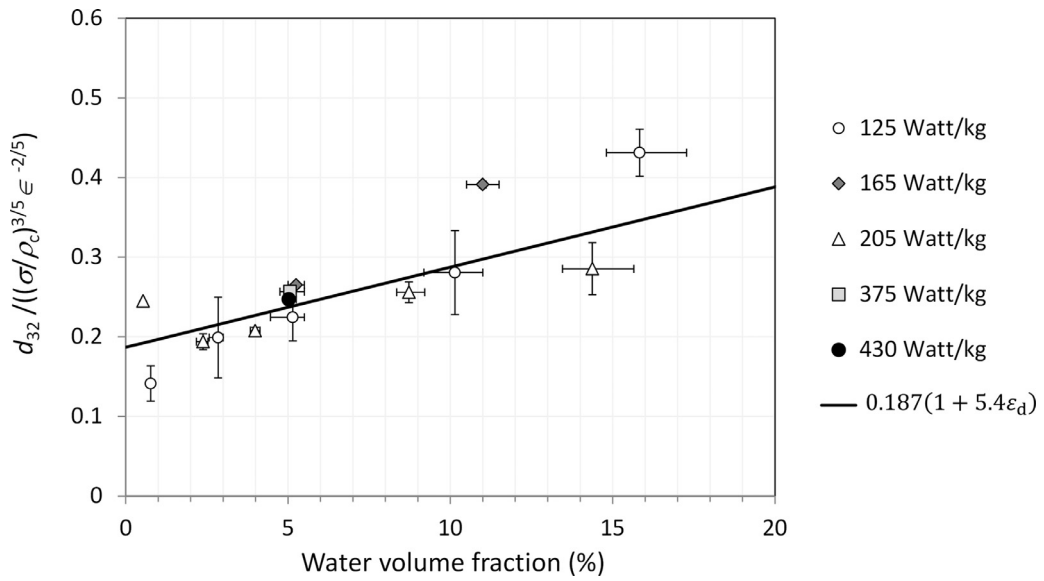
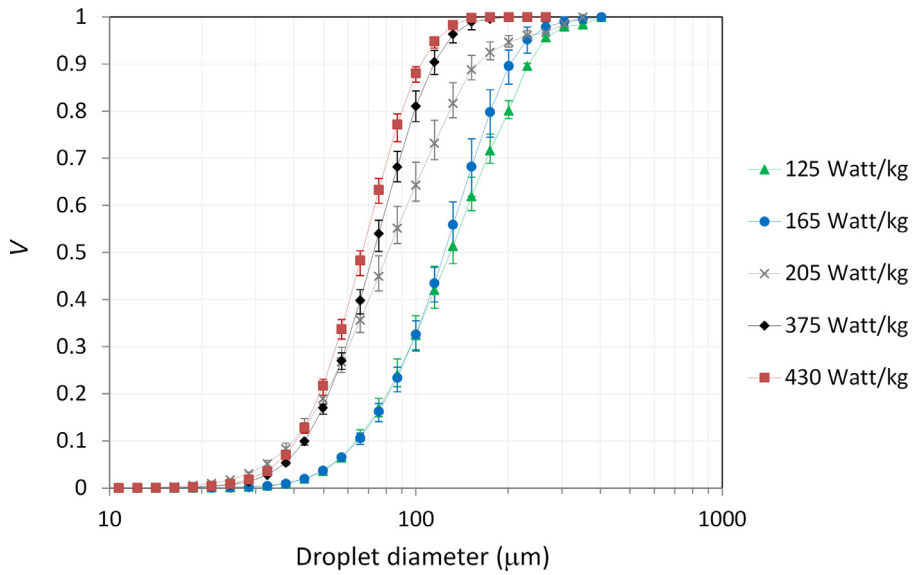**Fig. 13.** Measured normalized Sauter mean diameter as a function of the water volume fraction.

Fig. 14. Cumulative volume droplet size distribution for different mean energy dissipation rates and water volume fraction about 5%.
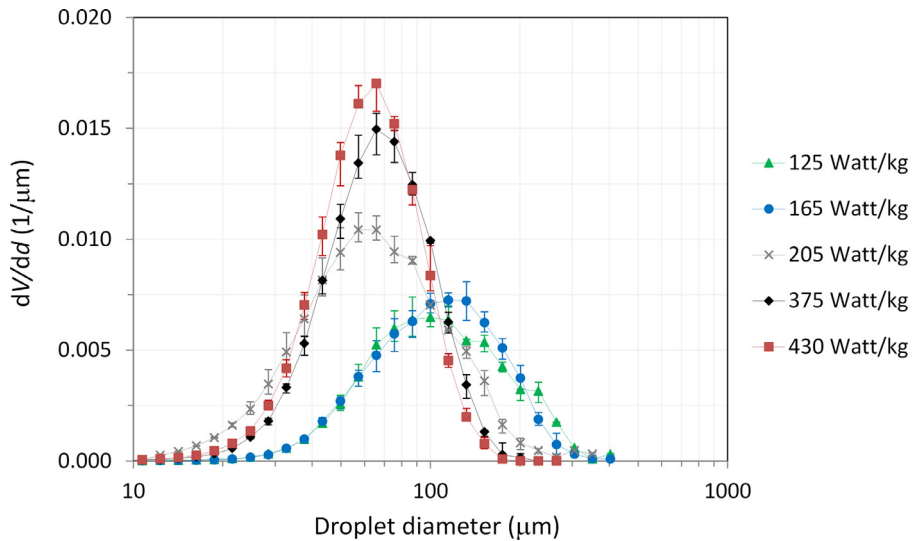

Fig. 15. Volume density droplet size distribution for different mean energy dissipation rates and water volume fraction about 5%.
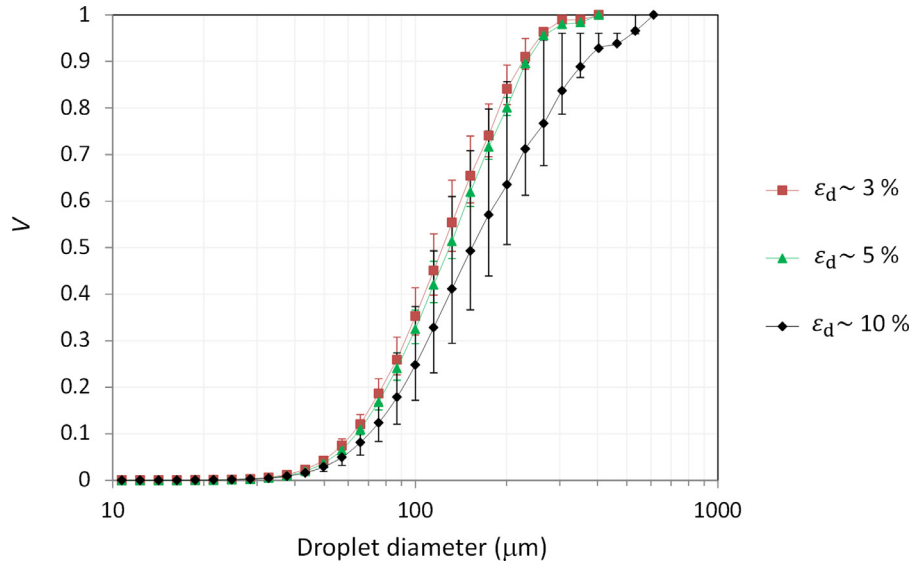
Fig. 16. Cumulative volume droplet size distribution for different water volume fractions and mean energy dissipation rate of about 125 W/kg.
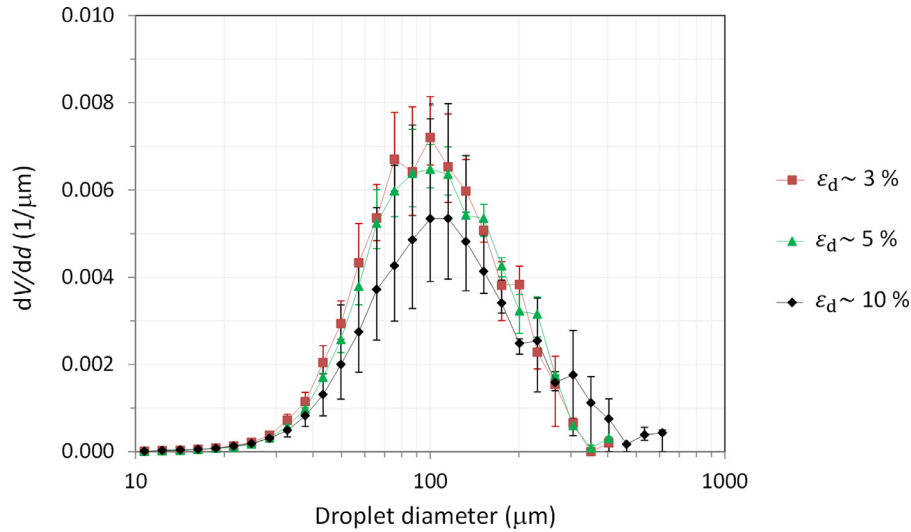
Fig. 17. Volume density droplet size distribution for different water volume fractions and mean energy dissipation rate of about 125 W/kg.

phase. Each shown distribution is the average of at least 3 different runs at the same experimental conditions, the error bars show the maximum and minimum obtained values. Droplet size distributions involve smaller droplet diameters, tend to be narrower, and the change in cumulative volume with droplet size is steeper with increasing mean energy dissipation rate. This is in line with the findings recently reported in an independent research work (Fossen and Schümann, 2017).

Figs. 16 and 17 show examples of cumulative volume and volume density droplet size distributions for different water volume fractions. Droplet size distributions seem to be slightly broader for larger water volume fractions, comprising more volume of droplets of larger sizes. Moreover, the change in cumulative volume with droplet size tends to be less pronounced with increasing water volume fraction.

Different statistical functions were used to model the obtained droplet size distributions. The Rosin–Rammler distribution (R–R) (Rosin and Rammler, 1933) has been extensively used due to its mathematical simplicity and is known to well represent droplet

sizes produced in oil–water pipe flow (Karabelas, 1978):

$$V = 1 - \exp\left[-\left(\frac{d}{d^*}\right)^n\right] \tag{35}$$

where V is the cumulative volume fraction of droplets with diameters lower than d, d^* is the droplet size characteristic of 63.2% of the total accumulated volume, and n is the exponent of the distribution.

The log-normal distribution (L-N) can be expressed as:

$$\frac{\mathrm{d}V}{\mathrm{d}d} = \frac{1}{d\sqrt{2\pi}\,\ln\sigma_{\mathrm{LN}}}\exp\left\{-\frac{1}{2}\left[\frac{\ln\left(d/\bar{d}\right)}{\ln\sigma_{\mathrm{LN}}}\right]^2\right\} \tag{36}$$

and as its integral form:

$$V = \frac{1}{2}\left\{1 + \mathrm{erf}\left[\frac{\ln\left(d/\bar{d}\right)}{\sqrt{2}\,\ln\sigma_{\mathrm{LN}}}\right]\right\} \tag{37}$$

where $\bar{d}$ is the logarithmic mean size of the distribution that represents 50% of the total accumulated volume (d_{50}), and σ_{LN} is the
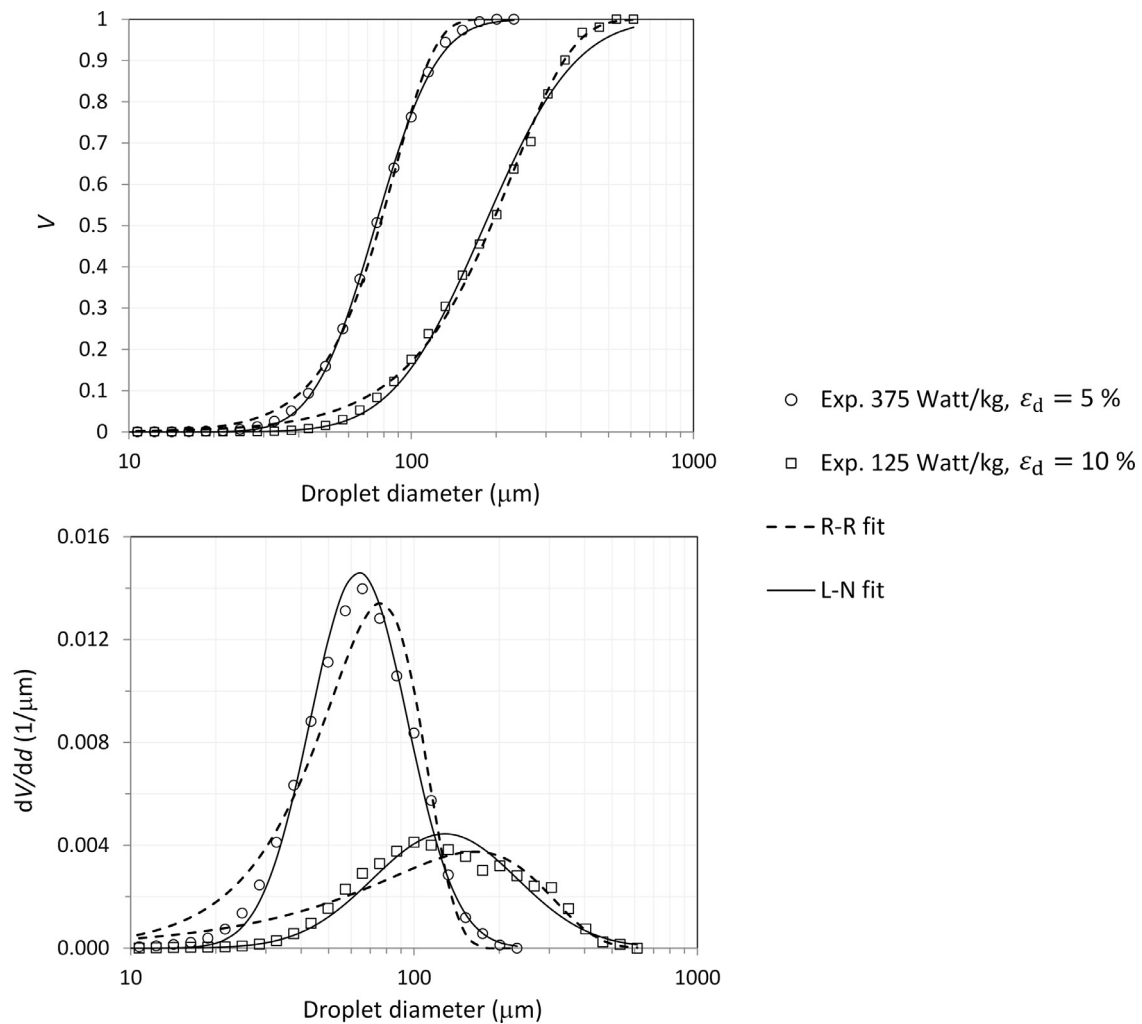
Fig. 18. Cumulative volume (top) and volume density (bottom) droplet size distribution examples for different experimental conditions showing R–R and L-N fit functions.

standard deviation that represents the width of the distribution and is equivalent to the ratio between d_{84} (84.1% of the cumulative volume) and d_{50}.

In general, the Rosin–Rammler and log-normal distributions both reasonably fit the cumulative volume experimental data as shown in Fig. 18 (top). On the other hand, the log-normal distribution offers a better fit on differential volume data (Fig. 18, bottom). The fitted curves and function parameters were obtained using non-linear least square methods with a coefficient of determination (R^2) always larger than 0.995 for all the fittings.

Fig. 19 shows the characteristic droplet size of the R–R distribution (d^*) normalized by the magnitude $(\sigma/\rho_c)^{3/5}\epsilon^{-2/5}$ as a function of the water volume fraction for all the tested conditions. The growth of the d^* with the water volume fraction can be fairly described using the Mlynek and Resnick function (Eq. (34)) multiplied by the constant 0.253 for best fit (solid line). The exponent n tends to increase with the mean energy dissipation rate (Fig. 20), showing values from about 2 to 3.4. The lower values represent wider distributions. The water content does not seem to affect significantly the values of n as can be inferred by comparing the data from water volume fractions lower and larger than 6% (white circles and grey squares, respectively). The determined n values are similar to the values of 2.1–3.1 reported by Karabelas (1978) and 2.3–2.8 reported by Angeli and Hewitt (2000), both established in water-in-oil turbulent pipe flow.

Fig. 21 shows the normalized values of the mean droplet size ($\bar{d}$) of the L-N distribution in function of the water volume fraction for all the tested conditions. The mean droplet size increases with the water volume fraction. Eq. (34) can also be used to model the trend. In this case, the best fit is obtained by multiplication with a constant of 0.212 (solid line). The standard deviation (σ_{LN}) tends to decrease with the mean energy dissipation rate, showing values from about 1.4 to 2 (Fig. 22). The values of σ_{LN} do not change considerably with the water volume fraction.

Fittings using R–R and L-N distributions were also performed on all the measured droplet size distributions filtered for residual water content. The obtained R–R distribution parameters d^* and n increased less than 10% and 6%, respectively; while the L-N distribution parameter $\bar{d}$ increased less than 10% and the standard deviation σ_{LN} decreased less than 8%. Again, as discussed above in Section 4.2, small differences are found between parameters characteristic of the droplet size distributions with and without considering residual water contamination.

4.5. General remarks

For the studied model oil and water system, it is demonstrated that maximum water droplet sizes generated by the used globe valve can be described fairly well by classic inertial turbulent break-up models, e.g., Hinze (1955), and also by specific mod-
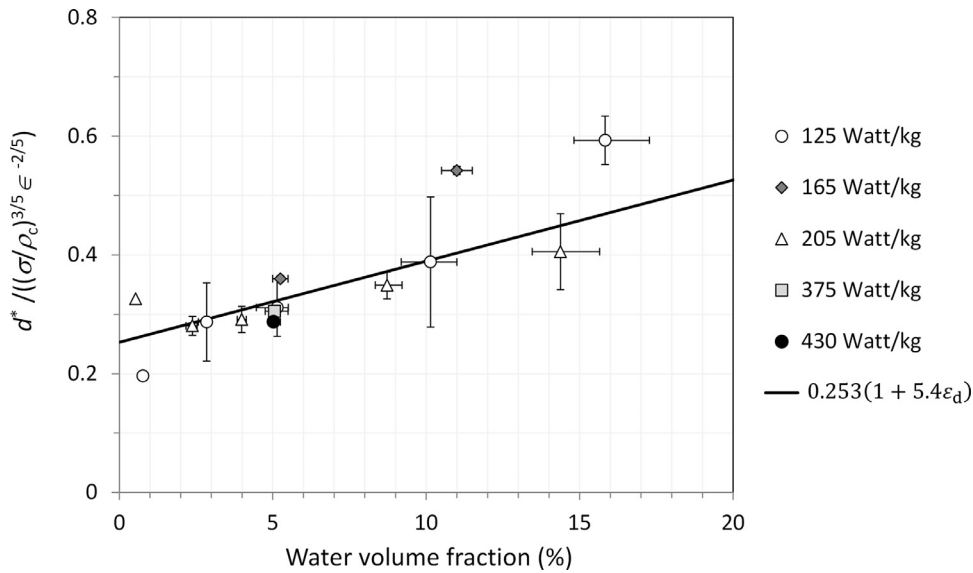
Fig. 19. Normalized fitted d^* values of the R–R distribution as a function of the water volume fraction.
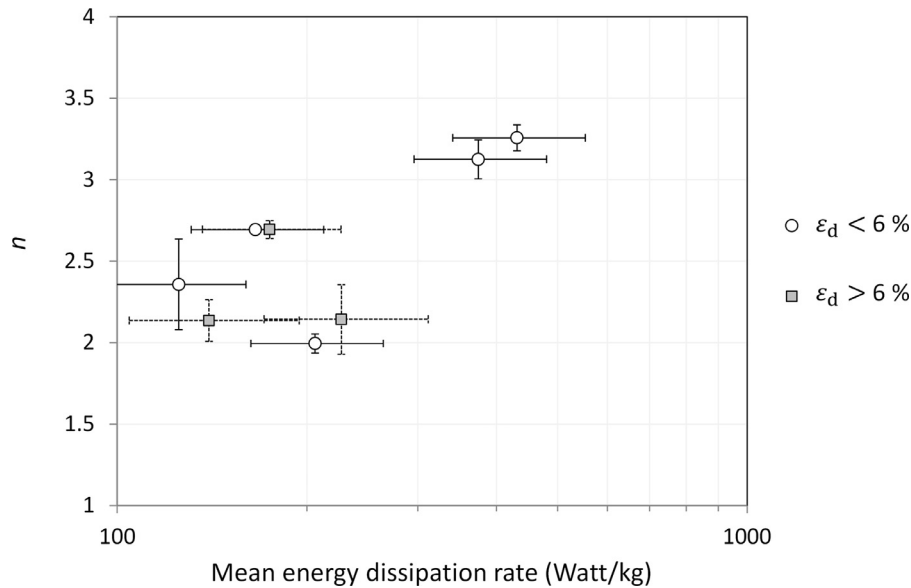

Fig. 20. Fitted values of the exponent n of the R–R distribution as a function of the mean energy dissipation rate.

els developed for turbulent break-up downstream from restrictions (Percy and Sleicher, 1983). Shear and elongation break-up mechanisms have been also evaluated using simple assumptions. In this case, it is found that these phenomena are not likely to regulate maximum droplet size. However, industrial processes are highly variable and, depending on the physicochemical properties of the used oil and water phases (e.g., density, viscosity and interfacial tension) and the intrinsic characteristics of the flow at the valve restriction (e.g., shear rate), the controlling droplet break-up mechanism may not be due to flow turbulence.

Measured droplet sizes are found to grow with the water volume fraction (ε_d). This trend can be fairly described using the empirical multiplication factor reported by Mlynek and Resnick (Eq. (34); Mlynek and Resnick, 1972). It is not clear either if turbulence damping or if coalescence related phenomena are responsible for this behavior. In the present case, the used oil and water system separates easily; thus, it might be thought that droplet coalescence mainly produces the observed droplet growth. How-

ever, similar trends of droplet size growth with the dispersed phase volume content have been reported in liquid–liquid systems with very poor coalescence as discussed elsewhere (Mlynek and Resnick, 1972; Pacek et al., 1998).

The average ratio between measured maximum and mean water droplet sizes is found to be about 3.7. Measured droplet size distributions show smaller droplet diameters and tend to be narrower with increasing the pressure drop across the valve and consequently the energy dissipated in the continuous phase. In this respect, the Rosin–Rammler and log-normal statistical functions can describe well the droplet size distributions in terms of cumulative volume. Although the characteristic droplet sizes d^* and $\bar{d}$ (from R–R and L–N functions, respectively) can be scaled accounting for the influence of turbulent flow and the fluid properties using Hinze's approach, the exponent of the R–R distribution (n) and the standard deviation of the L–N function (σ_{LN}) tend to vary with flow conditions. However, the available experimental data is insufficient to infer quantitative correlations with confidence. Average values
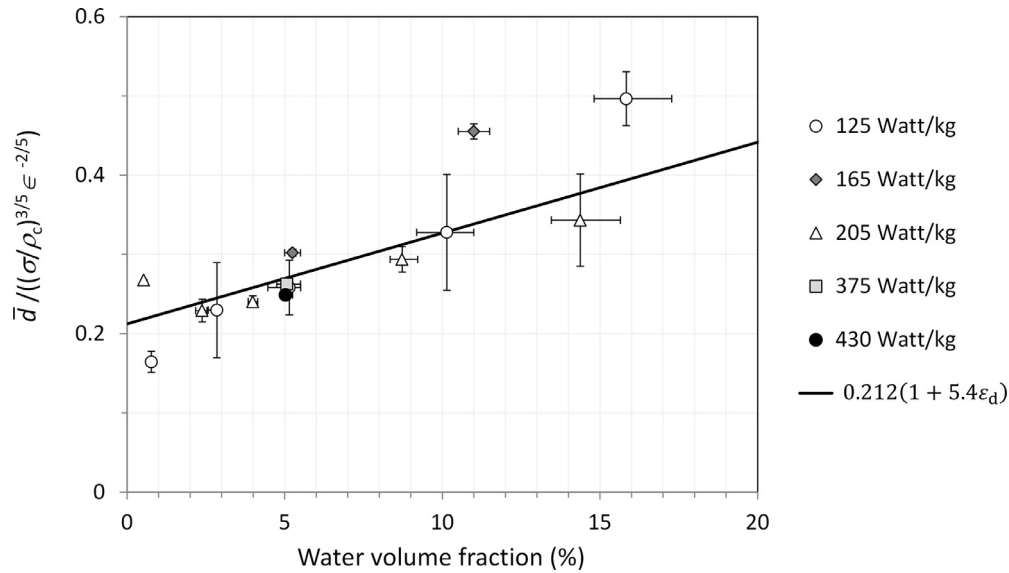
Fig. 21. Normalized fitted $\bar{d}$ values of the L-N distribution as a function of the water volume fraction.
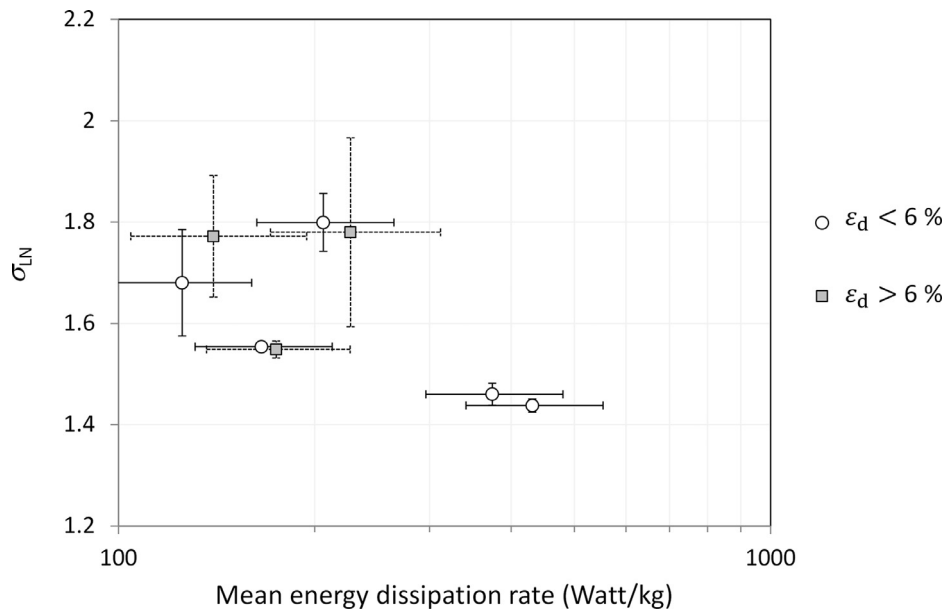

Fig. 22. Fitted values of the standard deviation σ_{LN} of the L-N distribution as a function of the mean energy dissipation rate.

of these parameters (e.g., $n \cong 2.68$ and $\sigma_{LN} \cong 1.59$) can be used instead to approximate droplet size distributions.

5. Conclusions

- Maximum water droplet sizes produced by the used globe valve in oil–water pipe flow tend to decrease with the mean energy dissipation rate of the continuous phase (ϵ). The found maximum droplet sizes are fairly well described by models of inertial turbulent break-up (e.g., Hinze's) that propose a dependency with ϵ of $-2/5$ power.
- The model proposed by Percy and Sleicher for orifice constrictions in pipes leads to reasonable predictions of maximum droplet size in dispersions with dispersed phase content below 6%, provided the geometry of the valve opening is known.
- Shear and elongation break-up mechanisms are evaluated at the valve opening using simple assumptions. It is found that these phenomena are not likely to control maximum droplet sizes.

- Sauter mean diameter also tend to decrease with the mean energy dissipation rate of the continuous phase. The average ratio between maximum droplet size and Sauter mean diameter is found to be about 3.7.
- Trends associated with maximum and mean droplet size growth with the water volume fraction (ε_d) can be fairly described in the tested range ($\varepsilon_d < 20\%$) using the empirical multiplication factor reported by Mlynek and Resnick.
- Droplet size distributions involve smaller droplet diameters and tend to be narrower with increasing the mean energy dissipation rate of the continuous phase. Besides, the increase of the water volume fraction broadens the distributions, comprising larger droplet sizes.
- Rosin–Rammler and log-normal statistical functions can both be used to represent fairly well the measured droplet size distributions in terms of cumulative volume. In particular, the log-normal distribution is more appropriate to represent differential volume data. Fitted parameters of the statistical

distributions are provided as a function of the tested flow characteristics.

Acknowledgments

References

Al-Otaibi, M., Elkamel, A., Al-Sahhaf, T., Ahmed, A.S., 2003. Experimental investigation of crude oil desalting and dehydration. Chem. Eng. Commun. 190, 65–82.

Angeli, P., Hewitt, G.F., 2000. Drop size distributions in horizontal oil–water dispersed flows. Chem. Eng. Sci. 55, 3133–3143.

Batchelor, G.K., 1951. Pressure fluctuations in isotropic turbulence. Math. Proc. Camb. Philos. Soc. 47, 359–374.

Bentley, B.J., Leal, L.G., 1986. An experimental investigation of drop deformation and breakup in steady, two-dimensional linear flows. J. Fluid Mech. 167, 241–283.

Boxall, J.A., Koh, C.A., Sloan, E.D., Sum, A.K., Wu, D.T., 2010. Measurement and calibration of droplet size distributions in water-in-oil emulsions by particle video microscope and a focused beam reflectance method. Ind. Eng. Chem. Res. 49, 1412–1418.

Brauner, N., 2001. The prediction of dispersed flows boundaries in liquid–liquid and gas–liquid systems. Int. J. Multiph. Flow 27, 885–910.

Cai, J., Li, C., Tang, X., Ayello, F., Richter, S., Nesic, S., 2012. Experimental study of water wetting in oil–water two phase flow—horizontal flow of model oil. Chem. Eng. Sci. 73, 334–344.

Calabrese, R.V., Chang, T.P.K., Dang, P.T., 1986. Drop breakup in turbulent stirred–tank contactors. Part I: effect of dispersed-phase viscosity. AIChE J. 32, 657–666.

Chern, M., Hsu, P., Cheng, Y., Tseng, P., Hu, C., 2013. Numerical study on cavitation occurrence in globe valve. J. Energy Eng. 139, 25–34.

Clay, P.H., 1940. The mechanism of emulsion formation in turbulent flow. I. Experimental part. Proc. R. Acad. Sci. 43, 852–865.

Collins, S.B., Knudsen, J.G., 1970. Drop size distributions produced by turbulent pipe flow of immiscible liquids. AIChE J. 16, 1072–1080.

Coulaloglou, C.A., Tavlarides, L.L., 1977. Description of interaction processes in agitated liquid–liquid dispersions. Chem. Eng. Sci. 32, 1289–1297.

Eow, J.S., Ghadiri, M., Sharif, A.O., Williams, T.J., 2001. Electrostatic enhancement of coalescence of water droplets in oil: a review of the current understanding. Chem. Eng. J. 84, 173–192.

Fossen, M., Schümann, H., 2017. Experimental study of the relative effect of pressure drop and flow rate on the droplet size downstream of a pipe restriction. J. Dispers. Sci. Technol. 38, 826–831.

Galinat, S., Garrido Torres, L., Masbernat, O., Guiraud, P., Risso, F., Dalmazzone, C., Noik, C., 2007. Breakup of a drop in a liquid–liquid pipe flow through an orifice. AIChE J. 53, 56–68.

Galinat, S., Masbernat, O., Guiraud, P., Dalmazzone, C., Noïk, C., 2005. Drop break-up in turbulent pipe flow downstream of a restriction. Chem. Eng. Sci. 60, 6511–6528.

Grace, H.P., 1982. Dispersion phenomena in high viscosity immisible fluid systems and application of static mixers as dispersion devices in such systems. Chem. Eng. Commun. 14, 225–277.

Hanzevack, E.L., Demetriou, G.D., 1989. Effect of velocity and pipeline configuration on dispersion in turbulent hydrocarbon-water flow using laser image processing. Int. J. Multiph. Flow 15, 985–996.

Hesketh, R.P., Etchells, A.W., Russell, T.W.F., 1991. Experimental observations of bubble breakage in turbulent flow. Ind. Eng. Chem. Res. 30, 835–841.

Hesketh, R.P., Fraser Russell, T.W., Etchells, A.W., 1987. Bubble size in horizontal pipelines. AIChE J. 33, 663–667.

Hinze, J.O., 1955. Fundamentals of the hydrodynamic mechanism of splitting in dispersion processes. AIChE J. 1, 289–295.

Hwang, C.-Y.J., Pal, R., 1998. Pressure losses in globe and gate valves during two-phase oil/water emulsion flow. Ind. Eng. Chem. Res. 37, 636–642.

Jansen, P.H., Noik, C., Dalmazzone, C., 2001. Emulsion formation in a model choke–valve. In: Proceedings of SPE Annual Technical Conference and Exhibition, SPE, New Orleans, LA SPE-71473-MS.

Karabelas, A.J., 1978. Droplet size spectra generated in turbulent pipe flow of dilute liquid/liquid dispersions. AIChE J. 24, 170–180.

Kubie, J., Gardner, G.C., 1977. Drop sizes and drop dispersion in straight horizontal tubes and in helical coils. Chem. Eng. Sci. 32, 195–202.

Lamb, H., 1932. Hydrodynamics. Dover Press, New York.

Levich, V.G., 1962. Physicochemical Hydrodynamics, 1st ed. Prentice-Hall, Englewood Cliffs, NJ.

Lovick, J., Mouza, A.A., Paras, S.V., Lye, G.J., Angeli, P., 2005. Drop size distribution in highly concentrated liquid–liquid dispersions using a light back scattering method. J. Chem. Technol. Biotechnol. 80, 545–552.

Mitre, J.F., Lage, P.L.C., Souza, M.A., Silva, E., Barca, L.F., Moraes, A.O.S., Coutinho, R.C.C., Fonseca, E.F., 2014. Droplet breakage and coalescence models for the flow of water-in-oil emulsions through a valve-like element. Chem. Eng. Res. Des. 92, 2493–2508.

Mlynek, Y., Resnick, W., 1972. Drop sizes in an agitated liquid–liquid system. AIChE J. 18, 122–127.

Pacek, A.W., Man, C.C., Nienow, A.W., 1998. On the Sauter mean diameter and size distributions in turbulent liquid/liquid dispersions in a stirred vessel. Chem. Eng. Sci. 53, 2005–2011.

Pal, R., Hwang, C.Y.J., 1999. Loss coefficients for flow of surfactant-stabilized emulsions through pipe components. Chem. Eng. Res. Des. 77, 685–691.

Palau-Salvador, G., Valverde, J.A., Frankel, S.H., 2004. Three-dimensional control valve with complex geometry: CFD modeling and experimental validation. In: Proceedings of the 34th AIAA Fluid Dynamics Conference and Exhibit. Portland, OR. AIAA.

Patel, V.C., Head, M.R., 1969. Some observations on skin friction and velocity profiles in fully developed pipe and channel flows. J. Fluid Mech. 38, 181–201.

Percy, J.S., Sleicher, C.A., 1983. Drop breakup in the flow of immiscible liquids through an orifice in a pipe. AIChE J. 29, 161–164.

Rammohan, S., Saseendran, S., Kumaraswamy, S., 2009. Numerical prediction and experimental verification of cavitation of globe type control valves. 7th International Symposium on Cavitation, CAV 2009, Ann Arbor MI, Paper 22.

Rosin, P., Rammler, E., 1933. The laws governing the fineness of powdered coal. J. Inst. Fuel 7, 29–36.

Sevik, M., Park, S.H., 1973. The splitting of drops and bubbles by turbulent fluid flow. J. Fluids Eng. 95, 53–60.

Simmons, M.J.H., Azzopardi, B.J., 2001. Drop size distributions in dispersed liquid–liquid pipe flow. Int. J. Multiph. Flow 27, 843–859.

Sleicher, C.A., 1962. Maximum stable drop size in turbulent flow. AIChE J. 8, 471–477.

Sprow, F.B., 1967. Distribution of drop sizes produced in turbulent liquid—liquid dispersion. Chem. Eng. Sci. 22, 435–442.

Stewart, M., Arnold, K., 2011. Surface Production Operations, Volume 1: Design of Oil Handling Systems and Facilities. 3rd ed, Gulf Professional Publishing, pp. 440–446.

Taylor, G.I., 1932. The viscosity of a fluid containing small drops of another fluid. Proc. R. Soc. Lond. Ser. A 138, 41–48.

Vafajoo, L., Ganjian, K., Fattahi, M., 2012. Influence of key parameters on crude oil desalting: an experimental and theoretical study. J. Petrol. Sci. Eng. 90–91, 107–111.

Vielma, M.A., Atmaca, S., Sarica, C., Zhang, H.-Q., 2008. Characterization of oil/water flows in horizontal pipes. SPE Proj. Facil. Constr. 3, 1–21.

van der Zande, M.J., van der Broek, W.M.G.T, 1998. Break-up of oil droplets in the production system. In: Proceedings of the ASME Energy Sources Technology Conference & Exhibition. Houston, TX. ASME ETCE98-4744.

van der Zande, M.J., van Heuven, K.R., Muntinga, J.H., van der Broek, W.M.G.T, 1999. Effect of flow through a choke valve on emulsion stability. In: Proceedings of SPE Annual Technical Conference and Exhibition. Houston, TX. SPE SPE-56640-MS.

Yang, Q., Zhang, Z., Liu, M., Hu, J., 2011. Numerical simulation of fluid flow inside the valve. Proc. Eng. 23, 543–550.